A Census of Dust and Gas Properties in Early-type Galaxies using the ALMA Archive

Benjamin J. Derieg

A senior thesis submitted to the faculty of
Brigham Young University
in partial fulfillment of the requirements for the degree of

Bachelor of Science

Benjamin Boizelle, Advisor

Department of Physics and Astronomy

Brigham Young University

ABSTRACT

A Census of Dust and Gas Properties in Early-type Galaxies using the ALMA Archive

Benjamin J. Derieg
Department of Physics and Astronomy, BYU
Bachelor of Science

Ongoing CO imaging with the Atacama Large Millimeter/submillimeter Array (ALMA) has probed molecular gas kinematics of circumnuclear disks (CNDs) in hundreds of local early-type galaxies (ETGs), providing the means for kinematic studies as well as those probing star formation and accretion processes. Here, we present results for a subset of these ALMA 12-m CO observations from Cycles 2 and 3 to build a census of circumnuclear gas and dust in ETGs at moderate angular resolution $\sim$0.25–1.0$''$. Our present sample of 27 galaxies contains a diverse set of CNDs that range in physical extent, gas mass, and kinematic properties, and which are observed at a range of inclination angles, angular resolutions, and sensitivities. We detail the process to construct moment maps and determine robust uncertainties in as homogeneous a manner as possible, followed by extraction of radial kinematic properties using KINEMETRY. These are supplemented by dust temperatures and masses obtained by fitting a modified blackbody to continuum data from both ALMA and other space-based IR observatories. The combination of these gas/dust properties provides a crucial cross-check, and, as expected, the gas-to-dust mass ratio is $\sim$100 for all galaxies in our sample. We also show that the CO kinematics generally align well with the larger-scale stellar distribution, although the difference in position angles is still $\gtrsim$10° for $\sim$50% of our sample, suggesting a moderate fraction of these CNDs may have external origin. A larger sample is still needed to confirm these results, and we discuss the application of the work here to all CNDs in the ALMA archive.

Keywords: Early-type galaxies (429), Galaxy kinematics (602), Molecular gas (1073), Dust continuum emission (412), Submillimeter astronomy (1647), Far infrared astronomy (529), Long baseline interferometry (932)

ACKNOWLEDGMENTS

I thank Dr. Benjamin Boizelle for his constant guidance during my time as an undergraduate, as well as the BYU College of Physical and Mathematical Sciences for funding this research. I'm also grateful to Nicholas LeVar for reducing large amounts of the data present in this work. I would also like to thank my parents and other family members who have offered me continual support throughout my time at BYU.

Contents

List of Figures

List of Tables

Chapter 1

Introduction

In the early 20th century, Hubble (1926) published his seminal paper classifying "extragalactic nebulae" into different types based on their morphology, starting the field of extragalactic astronomy. These galaxies, as they later came to be known, were originally divided into "early-type" and "late-type" galaxies (ETGs and LTGs, respectively). Though there were not originally many obvious reasons to organize them as such, it has become increasingly apparent in recent decades that galaxies of a similar morphology have similar formation mechanisms, stellar makeup, etc. In fact, a version of Hubble's classification is still used today as a useful scheme for organizing galaxies (de Vaucouleurs et al. 1991).

The LTG/ETG designations are further divided into several subclassifications. LTGs consist of both spiral and irregular galaxies. Spiral galaxies generally exhibit relatively flat stellar distributions with defined arms and central bulges. On the other hand, ETGs consist of elliptical and lenticular galaxies. Elliptical galaxies are typically redder than LTGs—indicating older stellar populations—and exhibit a more spheroidal shape with more random stellar motions. They also have less total gas and dust than LTGs, with more extended distributions. Lenticular galaxies display many of the same characteristics as ellipticals, but often with more defined features, and they represent a middle ground between elliptical galaxies and spiral galaxies.

In the decades following Hubble, increasingly powerful observational tools have allowed astronomers to get a better grasp on galaxy composition, structure, and evolution over time. For example, the development of radio, IR, and x-ray observatories allows one object to be observed at a variety of wavelengths—giving a fuller picture of emission properties—and highly-resolved spectral-line observations can give hints to the chemical makeup of an object. As a result, galaxy morphological classification has become significantly more nuanced. For example, radio observations have revealed previously unnoticed features stemming from active galactic nuclei (AGN), such as extended synchrotron jets (e.g., M87).

1.1 Circumnuclear Disks in Early-type Galaxies

While LTGs typically host larger gas reservoirs with regions of intense star formation, luminous ETGs were originally thought to be much smoother distributions of older stars, devoid of gas and dust. As our ability to resolve the interiors of luminous ETGs has increased, however, it has become clearer that this assumption is not completely correct. In fact, many ETGs do host significant atomic and/or molecular gas reservoirs. In these cases, ETGs provide an interesting case study of ISM because of their inherent regularity. For example, they exhibit ordered rotation, host older stellar populations, and have a more ordered magnetic field structure than LTGs. Atomic gas is detected in $\sim$30 percent of these (but much lower in cluster environments; e.g., di Serego Alighieri et al. 2007; Serra et al. 2012), while molecular gas is identified in somewhat greater than 20 percent of all ETGs (Alatalo et al. 2013; Young et al. 2011). In addition, coincident and cold dust ($\sim 20-40$ K) has been reported in between 20$-$25 percent of all elliptical galaxies, and nearly half of lenticulars (c.f. the higher values in di Serego Alighieri et al. 2013; Knapp et al. 1989; Kokusho et al. 2019; Temi et al. 2004). In perhaps 10 percent of all ETGs, these gas and dust reservoirs appear in the form of flat, mildly-warped, dusty circumnuclear disks (CNDs) with radii ranging from $\sim$ 100 parsecs (pc)

to a few kpc (1 pc $\approx$ 3.26 light-years). In this paper, I will focus on these regular CNDs, as they provide one of the most straightforward probes of how the interstellar medium (ISM) in a galaxy can interact with an AGN and thereby influence galaxy evolution.

1.1.1 Composition

One of the more important questions to ask about CNDs is: what are their compositional properties? In general, ISM consists of multiple phases across an entire galaxy. In ETGs, the total gas mass is dominated by molecular hydrogen (H_2), though there still exists a notable fraction of neutral atomic hydrogen (H I). Importantly, the atomic hydrogen distribution is often significantly more extended than that of the molecular hydrogen. Within the CND, Boizelle et al. (2017) estimate that atomic hydrogen should contribute at most $\sim 10^7\ M_\odot$, while the total molecular gas mass is typically on the order of a few $10^8\ M_\odot$. It is therefore reasonable to make the simplifying assumption that all gas in these CNDs is molecular in nature.

The molecular gas in CNDs is primarily H_2, but with a significant mass fraction of helium as well ($\sim$30–40 percent assuming a chemically-enriched ISM). There are also traces of other molecules, such as CO and HCO+, with some diffuse dust as well. From a sample of 260 ETGs, Kokusho et al. (2017) find a mass ratio of $M_{\rm dust}/M_{\rm H_2} = 0.0075$. On average, they find a cold dust temperature of 26 ± 6 K, with many ETGs having a minor warm dust component at 83 ± 22 K due to a radial temperature gradient with hotter dust closer to the center. However, a single-component (modified) blackbody typically describes the thermal dust emission well, and any warm dust contributes insignificantly to the total dust mass. Since the molecular gas and dust in CNDs is expected to be well-mixed, they have roughly the same temperature.

Even though dust is a relatively minor component of the CND mass, it has a significant effect on observation and plays an important role in evolutionary processes. First of all, CNDs can be detected at optical/IR wavelengths by dust obscuration of stellar light originating behind the CND

(see section 1.2). This obscuration has the effect of reprocessing some optical light into the far-IR as the emission is absorbed and re-emitted thermally by the dust. As such, dust is also seen prominently in the mid to far-IR. As will be discussed in the following section, even the relatively low dust mass ($\sim 10^4$–$10^6\ M_\odot$) is higher than expected. Along with the dust temperature, these hold clues to how the ISM in ETGs interacts with the host galaxy.

1.1.2 Role in Galaxy Evolution

As implied earlier, while it is not overly difficult to classify galaxies according to their morphology, it is quite a challenge to determine how they evolve over time (from internal mechanisms, galactic mergers, tidal disruption, etc.). Due to their small size, it may be easy to assume that CNDs do not play a significant role in such evolution. However, central supermassive black holes (SMBHs) do, despite being only $\sim$0.1 percent the mass of the stellar bulge of a typical galaxy (Kormendy & Ho 2013). For example, a tight correlation between SMBH mass and central stellar velocity dispersion has been observed, suggesting their coevolution over long timescales through processes such as mergers and star formation (van den Bosch 2016). SMBHs in the form of luminous AGN—from accretion of nearby material onto the black hole—also drive feedback, where thermal emission from the AGN heats the surrounding gas, thereby influencing local star formation. Strong magnetic fields from an AGN can also drive relativistic jets which suppress star formation in their own right.

Due to their proximity to the galactic nucleus, the composition and morphology of a CND also play a part in galaxy evolution. Nevertheless, their exact role is not well understood. Perhaps the first key is to ask where they come from. Because of their regularity, it was initially assumed that they formed *in situ*. However, several recent studies have given evidence to the contrary. Misaligned, disturbed, and filamentary dust features would be consistent with either cold-mode accretion or merger events that have yet to fully settle down into a galaxy's midplane (e.g., Tran et al. 2001), a process that may take several hundred Myr (or longer; see van de Voort et al. 2015).

Likewise, gas kinematics that are significantly misaligned with its host galaxy's stellar kinematics (and occassionally anti-aligned; Davis & Bureau 2016) provide strong evidence for external origins. Disk warping may also herald ongoing accretion onto otherwise relaxed gaseous disks. Due to the prevalence of significant misalignments between gaseous and stellar kinematics, Davis et al. (2011) estimate that the CNDs in nearly half of nearby ETGs are externally generated. However, dust destruction is expected to proceed rapidly during the accretion and/or merger processes, with calculations of X-ray sputtering in the hot halos of many massive ETGs suggesting survival timescales as short as 1 Myr (Draine & Salpeter 1979) and as long as 100 Myr (Clemens et al. 2010). Kokusho et al. (2019) find no apparent correlation between the total dust mass in ETGs and the masses of the evolved stellar population, suggesting either inefficient grain production or efficient destruction. Certainly, the details of dust shielding and generation are not sufficiently well understood to explain the apparent longevity of grains in misaligned CNDs.

On the other hand, there is some evidence for internal formation (or at least retention) mechanisms for a fraction of CNDs. Using the Combined Array for Research in Millimeter-wave Astronomy (CARMA; Bock 2006) for a survey of ATLAS^{3D} ETGs, Alatalo et al. (2013) find that molecular gas kinematics are preferentially aligned with stellar kinematics. This resolved kinematic analysis was limited to the most massive CNDs, but for this subsample, the gas kinematics remain consistent with an internal origin. Another argument in favor of *in situ* formation is that the inferred gas reservoirs in ETGs (from observations of both dust and molecular gas; ranging from about 10^5 to a little above 10^9 $M_\odot$; Boizelle et al. 2017; Kokusho et al. 2019; Young et al. 2011) may exceed the amount that could be retained—and not consumed in star formation—in a typical minor merger with all but the most gas-rich dwarf galaxies (with most dwarf galaxies having $\lesssim 10^9$ $M_\odot$ of total gas; e.g., Leroy et al. 2005; Putman et al. 2021). These massive CNDs are seen almost exclusively in lenticular galaxies, at times even exceeding 10^9 $M_\odot$ in molecular gas (Young et al. 2011). They may be remnants of old gaseous disks. In these cases, very low star formation rates were likely

driven by high velocity gradients during the growth of the stellar bulge, which shears clouds apart before they can collapse to form stars (i.e., morphological quenching; Martig et al. 2013).

At any rate, it is evident that a better understanding of CND gas kinematics, dust/gas masses, dust/gas temperatures, and other statistical properties will give an idea of their origins. In turn, understanding where they come from and how they are retained will give a fuller picture of galaxy evolution and the role the galactic nucleus plays therein.

1.2 Observations of Circumnuclear Disks

Having established the existence of CNDs, as well as their key role in probing galaxy evolution, I now turn to how they are observed. The most obvious and longest-known method of observing CNDs is by the dust's obscuration of background stars at optical wavelengths. While dust makes up only a small component of the ISM, the grains themselves are much larger than gas molecules—having radii up to $\sim$1 μm—and thus contribute to significant extinction and reddening (Draine 1989). Observations of dust obscuration inform our understanding of CND morphology: they are generally very flat, uniform, and show some evidence of a central depression (i.e., lack of molecular material towards the center). Nevertheless, such observations offer little in terms of quantitative measures of the ISM properties.

On the other hand, the dust, being in thermal equilibrium, can be seen in continuum emission with a blackbody peak around 100 μm (corresponding to a temperature of $\sim$ 20–30 K, as discussed). At these wavelengths, there is little contamination from other sources, so thermal dust emission dominates the total galaxy continuum. At both the short ($\lambda \lesssim 10$ μm) and long ($\lambda \gtrsim 1$ mm) wavelength extremes of this blackbody emission, stellar continuum and AGN synchrotron emission, respectively, begin to dominate the spectral energy distribution (SED). Because the dust is opaque, it is not a perfect blackbody, but rather is better described by a so-called "modified" blackbody that

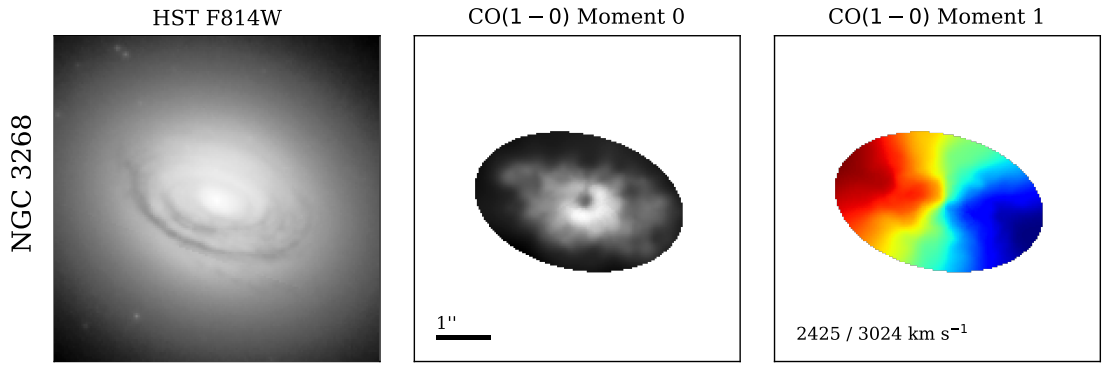

Figure 1.1 An example of the CND in NGC 3268. From left to right: HST F814W ($\lambda \sim 810$ nm) image, CO moment 0, and CO moment 1 maps. The same spatial scale and orientation is retained for each image. Notice the central hole in the CO brightness ($\sim$50–60 pc in diameter), and that the gas and dust are well aligned. Velocity minima/maxima are listed on the moment 1 map, with the galaxy recessional velocity being $\sim$2725 km s^{-1}.

accounts for self-absorption (see the full details in section 2.5.2). In this mid to far-IR regime, the thermal dust in CNDs is best seen with space-based observatories like IRAS, Herschel, and Spitzer. However, poor angular resolution at far-IR wavelengths ($\sim$ 5–40$''$) relative to the arcsecond-scale disks means that the typical CND cannot be resolved. As such, the thermal emission from the CND can only be seen averaged together with emission from grains that are sparsely distributed over the entire galaxy. This is one limitation of constraining CND properties with thermal dust observations: parameters like total dust mass may be overestimated due to contamination from more extended dust features. Additionally, it can be difficult to fill out the spectrum with enough data points to accurately constrain the blackbody parameters because multiple observatories must be used, ranging from millimeter to micron wavelengths.

The next logical place to look for CND emission is from the molecular gas. Given its symmetry and lack of a permanent dipole moment, H_2 itself is difficult to observe since the lowest-energy lines are found at mid to near-IR wavelengths in gases of 1000–2000 K. The next most abundant molecule, CO (which is well-mixed into the CND with a CO-to-H_2 abundance ratio of $\sim 3.2 \times 10^{-4}$; Bolatto et al. 2013), can be used as a tracer of the whole gas reservoir. CO makes for a good tracer

due to its strong rotational emission lines—for example, the CO(1−0) (at $\nu_{\rm rest} = 114.222$ GHz) or CO(2−1) (at $\nu_{\rm rest} = 228.439$ GHz) lines[1]—with upper levels that are efficiently populated at low temperatures (20–30 K) in a moderately dense environment ($n_{\rm H_2} \sim 2000$ cm^{-3}). In section 2.4, we discuss the conversion of the total strength of such lines over the whole disk into a total gas mass. Additionally, resolved emission-line observations reveal the gas kinematics. Because a CND is typically seen inclined relative to the observer at some angle i, and rotating about the galactic center (at circular velocities of up to ~ 1000 km s^{-1} at the center), the radial velocity of the line can be spatially mapped. As we discuss in section 3.1, spectral-line observations suffer from the same limitations arising from finite angular resolution and measurement uncertainty as any other observation.

1.2.1 Previous ETG CO Surveys

Several surveys have measured molecular gas properties (both resolved and unresolved) for large ETG samples. The two I will discuss here are primarily dynamical surveys, though other surveys have focused on non-kinematic properties (e.g., dust emission in Kokusho et al. 2017).

The Spectroscopic Areal Unit for Research on Optical Nebulae (SAURON) survey selected a representative set of 72 ETGs (comprising E, S0, and Sa types) to look at gas and stellar kinematics (de Zeeuw et al. 2002). Primary observations were taken with an integral field spectrograph (IFS), which takes a large number of optical spectra at positions across the field of view to form a so-called "data cube"—a set of images at closely-spaced frequencies (Bacon et al. 2001; Combes et al. 2007). Major results of this early survey include that: dust features are always accompanied by atomic gas emission, but not vice-versa; atomic gas kinematics are preferentially aligned with the host galaxy's stellar kinematics, which is inconsistent with a purely external origin (though such misalignment may be dependent on the level of apparent inclination; Sarzi et al. 2006); and low gas velocity

[1] CO(1−0) indicating, for example, transition from the $J = 1 \rightarrow 0$ state

dispersion is linked with high star formation rates, indicating that stars are generally formed from dynamically cold gas (Falcón-Barroso et al. 2006). Unfortunately, the molecular gas kinematics were not resolved due to limitations in telescope capabilities at the time.

More recently, the larger, volume-limited ATLAS^{3D} survey again looked at a sample of 260 ETGs (E and S0 types) with the SAURON instrument in the optical, while obtaining more extensive and higher angular-resolution CO imaging at mm wavelengths (Cappellari et al. 2011). They provide a statistically representative sample of all ETGs within 42 Mpc. CO emission was detected in 22 percent of the sample (Young et al. 2011), and a significantly higher fraction (36 ± 5 percent) were found to have kinematic misalignment (Davis et al. 2011). Molecular gas content does not depend on the kinematic misalignment, but the cluster environment is correlated with total gas mass. For example, Virgo cluster members are found to have less extended molecular gas reservoirs (Davis et al. 2013).

1.2.2 Using ALMA to Observe Circumnuclear Disks

Previous ETG surveys were limited in their ability to study molecular gas properties due to low sensitivity or poor angular resolution. The recently completed Atacama Large Millimeter/submillimeter Array (ALMA) offers an order-of-magnitude improvement on both of these over previous observatories. This interferometric array in Chile consists of a main array of sixty-four 12-m diameter antennas in multiple configurations ranging in size from 0.15 to 18 km, as well as the ALMA Compact Array (ACA), which is made up of four 12-m and twelve 7-m antennas with a combined collecting area equivalent to that of $\sim$ 50-m dish (Tarenghi 2008). Long baselines reaching up to 15 km separations, combined with the compact array, gives ALMA the ability to create continuum and spectral-line images at a variety of scales. In extended-array configurations, angular resolutions of less than $0.01''$ can be achieved.

Recently, ALMA has facilitated sensitive and high angular resolution CO imaging in an ever-growing sample of $\gtrsim$100 ETGs with CNDs. These ALMA data sets allow for the mapping of molecular gas properties and kinematics in exquisite detail. Many of these observations have been primarily explored for general gas properties, including cloud statistics (e.g., Liu et al. 2021; Utomo et al. 2015), star formation and stability arguments (e.g., Hirota et al. 2018; Utomo et al. 2017; 2018), and the feeding of AGN (e.g., Ruffa et al. 2019a;b). In cases where the molecular gas traces the circular rotation pattern close to the central SMBH (typically down to scales of $\sim$10–50 pc), gas-dynamical modeling can recover highly precise measurements of the SMBH mass (e.g., Barth et al. 2016; Boizelle et al. 2019; 2021; North et al. 2019). This method of SMBH mass measurement does not suffer from many of the serious uncertainties inherent in other techniques. For example, dust obscuration at mm wavelengths is not a problem such as in the case of stellar dynamical modeling; also, a much larger fraction of galaxies host CNDs as compared to, for example, megamaser disks (which can also probe SMBH mass).

Many of these archival CO emission-line data sets remain underutilized for the purpose of surveying molecular gas properties in ETGs, but the quality of the data exceeds that accomplished by SAURON or ATLAS^{3D}, and can help answer the questions posed in the previous sections. Additionally, the location of ALMA in the southern hemisphere means it has observed many targets which could not be included in other surveys. Here, I present the beginnings of a long-term project to census the dust and gas properties of a large number of CNDs whose observations already exist in the ALMA science archive. As mentioned, over 100 such observations exist, but I focus on a subset of 27 in order to refine the methods for data reduction and analysis. The selection of this subsample is described in chapter 2, after which I detail the methods for data reduction and kinematic analysis (as well as looking at total gas mass, surface brightness profiles, etc.). I also describe ALMA and IR continuum measurements, along with SED fitting to determine dust masses and temperatures as described in Kokusho et al. (2017), with the addition of ALMA continuum data to better constrain

the red end of the blackbody fit. The combination of all this data will then be used in chapter 3 to discuss some preliminary statistics/properties of the sample (e.g., kinematic misalignment compared with the ATLAS^{3D} galaxies). Some general conclusions and takeaways will then be introduced, and I will discuss the future of this project, and how these methods will be applied to the entire ALMA archive. Summaries of each target are also given in appendix B.

Chapter 2

Data and Methods

The primary data sets in this project consist of interferometric observations made with the ALMA observatory, all of which is publicly available on the ALMA science archive website[1]. To ensure uniformity in our sample, we neglect the pipeline-calibrated data in favor of performing self-calibration and imaging ourselves. In section 2.1, I detail the sample selection process. This is followed by a description of the process of reducing the ALMA data and imaging both the continuum and CO emission in section 2.2. In section 2.3 I demonstrate the construction of moment maps and uncertainties from the ALMA data, and introduce the KINEMETRY code to quantify the disk kinematics. Finally, I give a brief overview in section 2.5 of how ALMA continuum images were used (along with photometric data from other infrared observatories) to constrain CND dust properties in our sample.

2.1 Sample Selection

In its 10 years of operation, ALMA has imaged everything from solar system objects, to protostellar nebulae, to the earliest galaxies. Here, we focus on the $\gtrsim$100 distinct ETGs with regular, dusty

[1] https://almascience.nrao.edu/aq/

CNDs that have been observed to study continuum emission and spectral-line behavior. At the present moment, we restrict ourselves to ETGs observed as part of cycles 3 and earlier (primarily obtained mid-2014 to late 2016), with a few additional observations of the same targets from later cycles included for comparison. This allows us to focus on a more careful analysis before applying these methods to the whole sample. Data from earlier ALMA cycles also took up less space (a few GB per target compared to hundreds of GB), and therefore takes significantly less time to calibrate.

For each ETG in this set, we use the quick-look feature on the ALMA science archive website to determine if there are any detected spectral-line features. For an initial sample of 106 ETGs observed in cycles 1–3, we select only targets which: (1) have reasonably resolved CO emission features (in both the spatial and frequency dimensions); (2) have dynamically cold CNDs (i.e., they appear to be regularly rotating); and (3) are not so extended as to reach outside the FOV. Applying these criteria leads to a sample of 27 ETGs. Table 2.1 contains some basic properties of these targets.

2.2 ALMA Data Reduction

For each target, the raw visibilities (*uv* data), imaging scripts, and calibration tables were obtained from the ALMA archive and a calibrated measurement set (MS; including all flagging) was recovered using a pipeline script and some manual additions using the Common Astronomy Software Applications (CASA; CASA Team et al. 2022). After selecting only those spectral windows corresponding to the bright continuum and line emission, we performed image deconvolution using the TCLEAN task to transform between visibilities and image-plane intensity maps. Most of the targets have a bright continuum source, so we applied phase and amplitude self-calibration to correct for atmospheric changes that occur on minute timescales, as well as improve the dynamical range

Table 2.1. Sample Parameters

Galaxy (1)	RC3 Type (2)	z (3)	D_L (Mpc) (4)	Ang. Scale (pc/arcsec) (5)	σ_* (km s^{-1}) (6)	$M_{\rm BH}$ ($10^7\ M_\odot$) (7)
NGC 1332	S0	0.0054	22.91 (1.98)[b]	109.9	294.6	162.4
NGC 1380	SA0	0.00626	17.62 (1.52)[b]	84.4	214.5	29.7
NGC 3258	E1	0.0096	32.06 (4.25)[b]	152.5	261.0	85.0
NGC 3268	E2	0.00934	34.83 (4.25)[b]	165.7	228.6	41.8
NGC 6861	SA0	0.00944	28.05 (5.06)[b]	133.5	387.2	701.0
NGC 0997	E	0.02169	92.92 (6.53)[a]	431.6	···	···
NGC 1684	cD	0.01484	62.78 (2.32)[d]	295.5	273.8	109.7
NGC 5208	S0	0.02269	110.07 (7.7)[a]	510.2	···	···
NGC 0383	SA0	0.017	66.1 (2.61)[d]	309.8	272.9	107.8
NGC 0524	SA0	0.00802	23.99 (2.31)[b]	114.5	236.7	50.3
NGC 6958	cD	0.00905	43.12 (3.02)[a]	205.3	185.2	13.6
NGC 1386	SB0	0.0029	16.52 (2.02)[b]	79.6	133.1	2.3
NGC 1387	SAB0	0.00626	20.32 (2.59)[b]	97.3	167.3	7.9
NGC 0708	E	0.01589	61.52 (2.45)[d]	289.0	221.8	35.5
NGC 3607	SA0	0.0031	22.8 (1.86)[b]	109.9	222.2	35.9
NGC 3862	E	0.02159	103.48 (7.24)[a]	480.7	265.1	92.3
NGC 4061	E	0.02445	104.07 (1.44)[c]	480.7	477.2	2142.2
NGC 4435	SB0	0.00264	16.65 (0.52)[e]	80.3	155.0	5.2
NGC 4438	SA0	0.00024	16.65 (0.52)[f]	80.7	135.3	2.5
PGC 43387	E1	0.02285	109.52 (7.67)[a]	507.5	213.5	29.0
NGC 3557	E3	0.01027	45.71 (4.87)[b]	217.1	270.3	102.3
NGC 4697	E6	0.00414	11.75 (0.78)[b]	56.5	165.2	7.4
NGC 4786	cD	0.0151	75.68 (5.3)[a]	356.1	284.7	135.2
NGC 5838	SA0	0.00418	23.96 (1.68)[a]	115.2	273.6	109.2
NGC 4477	SB0	0.00446	15.05 (1.06)[a]	72.3	172.5	9.3
NGC 4596	SB0	0.00631	14.88 (1.04)[a]	71.2	140.6	3.1

Note. — Col. (2): from the RC3 catalog (de Vaucouleurs et al. 1991). Col. (3): redshift (z) averaged from NED. Col. (4): luminosity distance from the referenced source (with uncertainty). Col. (5): factor for conversion from angular units on the sky to a physical scale. Col. (6): from the HyperLEDA catalog (Makarov et al. 2014). Col. (7): BH mass derived from the $M_{\rm BH} - \sigma_*$ relation according to van den Bosch (2016).

(a): derived from NED redshift (Virgo + GA + Shapley)

(b): Tonry et al. (2001)

(c): Mandel et al. (2011) adjusted for Virgo + GA + Shapley

(d): Jensen et al. (2021)

(e): Blakeslee et al. (2009)

(f): same as NGC 4435 due to proximity

(peak/noise) using the GAINCAL and APPLYCAL tasks. This level of self-calibration was only done on targets for which improvement in the dynamic range was seen.

We next fit the continuum emission from all line-free spectral windows in the *uv* (Fourier) plane, and subtracted this off from the data. This was done with the UVCONTSUB task in CASA. Finally, after continuum subtraction, the spectral window(s) containing the line emission were deconvolved in TCLEAN one more time into a frequency-resolved data cube consisting of two spatial (sky) coordinates and one frequency axis. This deconvolution was performed using Briggs weighting (Briggs 1995) with robustness parameter $r = 0.5$ to strike a balance between sensitivity and spatial resolution.

The data used here have an average beam FWHM of $0.62''$, corresponding to typical spatial resolutions of a few tens of pc at the source. The final, calibrated emission-line data cubes have velocity channel widths ranging from 9.9–40.5 km s^{-1} and an average RMS background sensitivity of 1.35 mJy beam^{-1} per channel. Velocities were calculated using the optical definition in the barycentric frame of reference. The specific details for each observation are given in table 2.2.

In addition to CO-line data cubes, we also image the continuum emission from each target. This is done in two ways: first, the total continuum is imaged by TCLEAN deconvolution after self-calibration, as described earlier. However, most of the targets have a bright, unresolved, nuclear continuum source from an AGN (from either thermal, free-free, or synchrotron emission). This presents difficulty when attempting to measure the extended dust continuum brightness, since the extended surface brightness is much lower than the AGN emission—especially in ALMA bands 3–7 which lie very far down the Rayleigh-Jeans tail for dust in the 10–50 K range. To work around this, we model the nuclear continuum as a point source in the *uv* plane using the UVMODELFIT task in CASA, and subtract this central source from the MS with UVSUB before re-imaging the continuum intensities. This leaves only the thermal dust emission; see Fig. 2.2 as an example.

Table 2.2. Observational Details

Project Code (1)	Galaxy (2)	CO Transition (3)	Int. Time (min) (4)	Δv (km s^{-1}) (5)	$\theta_{maj}/\theta_{min}$ (arcsec) (6)	RMS Noise (mJy beam^{-1}) (7)
			Cycle 2			
2013.1.00229.S	NGC 1332	2−1	21.7	19.9	0.32/0.23	0.457
2013.1.00229.S	NGC 1380	2−1	44.4	19.9	0.23/0.18	0.498
2013.1.00229.S	NGC 3258	2−1	44.4	19.8	0.48/0.4	0.392
2013.1.00229.S	NGC 3268	2−1	44.4	19.8	0.45/0.4	0.427
2013.1.00229.S	NGC 6861	2−1	23.2	19.8	0.32/0.23	0.54
			Cycle 3			
2015.1.00187.S	NGC 0997	2−1	12.6	9.9	0.32/0.26	1.29
2015.1.00187.S	NGC 1684	2−1	8.1	10.0	1.03/0.77	2.54
2015.1.00187.S	NGC 5208	2−1	10.6	9.9	0.85/0.076	2.43
2015.1.00419.S	NGC 0383	2−1	2.0	20.0	0.9/0.59	1.99
2015.1.00466.S	NGC 0524	2−1	81.6	20.2	0.46/0.34	0.554
2015.1.00466.S	NGC 6958	2−1	4.0	20.1	0.042/0.024	0.525
2015.1.00497.S	NGC 1386	1−0	3.5	20.3	2.85/1.94	4.25
2015.1.00497.S	NGC 1387	1−0	3.5	10.1	2.85/1.94	4.06
2015.1.00598.S	NGC 0708	2−1	11.1	20.0	0.86/0.53	0.726
2015.1.00598.S	NGC 3607	2−1	10.6	39.9	0.67/0.55	1.72
2015.1.00598.S	NGC 3862	2−1	10.6	9.9	0.71/0.56	1.94
2015.1.00598.S	NGC 4061	2−1	10.6	19.8	1.15/0.63	1.77
2015.1.00598.S	NGC 4435	2−1	10.1	10.1	0.63/0.53	1.87
2015.1.00598.S	NGC 4438	2−1	10.1	10.2	0.61/0.54	5.13
2015.1.00598.S	PGC 43387	2−1	11.6	29.2	0.77/0.53	0.814
2015.1.00878.S	NGC 3557	2−1	19.7	20.1	0.37/0.27	0.431
2015.1.00878.S	NGC 4697	2−1	20.7	20.2	0.29/0.27	0.485
2015.1.00878.S	NGC 4786	2−1	20.2	20.0	0.28/0.26	0.456
2015.1.00878.S	NGC 5838	2−1	42.3	20.2	0.5/0.31	0.566
2015.1.00896.S	NGC 1332	2−1	104.9	20.2	0.041/0.025	0.19
2015.1.00989.S	NGC 4477	1−0	21.7	40.5	1.91/1.02	1.09
2015.1.00989.S	NGC 4596	1−0	19.2	20.2	1.79/1.02	1.57
2015.1.01572.S	NGC 3557	2−1	22.7	20.1	0.55/0.49	0.65
			Cycle 4			
2016.1.01135.S	NGC 6861	3−2	49.4	26.8	0.26/0.2	0.543
			Cycle 5			
2017.1.00301.S	NGC 4435	2−1	66.5	10.1	0.38/0.34	0.638

Note. — Observational properties for ALMA data CO cubes used in this project. Col. (3): rotational CO emission line used for moment maps. Col. (4): total on-source integration time for this observation. Col. (5): velocity binning of the cleaned/calibrated data cube. Col. (6): beam major/minor axis. Col. (7): RMS of the masked regions of the data cube.

2.3 Molecular Gas Kinematics

It is difficult to extract any meaning from a data cube alone. Rather, a data cube can be reduced in several ways to make the data more manageable. In this section, I describe the process of creating velocity maps from data cubes by collapsing them along the frequency axis. These can then be analyzed with a sort of Fourier decomposition (using the KINEMETRY code) to get at the kinematics of a CND as a function of radius. Such a decomposition quantifies disk circular velocity, deviation from circular rotation, and warping.

2.3.1 Velocity Moment Creation

A data cube can be thought of as consisting of one spectrum (in the frequency direction) at each pixel, and each spectrum carries information about the CO gas along that line of sight. Specifically, each moment of a spectrum has a physical meaning which samples some component of the gas phase-space density or distribution function. For example, the zeroth moment of a spectrum (i.e., the area under the curve) gives the total intensity at that location. Similarly, moment 1 (mean) and moment 2 (standard deviation) give the line-of-sight mean velocity and line-of-sight velocity dispersion, respectively. Formally, the first three moments of a distribution are given as

$$M_0 = \sum_i^N I_i \Delta v_{\mathrm{chan},i}, \tag{2.1}$$

$$M_1 = \frac{\sum_i^N I_i v_i}{\sum_i^N I_i}, \tag{2.2}$$

$$M_2 = \sqrt{\frac{\sum_i^N I_i (v_i - M_1)^2}{\sum_i^N I_i}}, \tag{2.3}$$

where I_i is the intensity, v_i the velocity, and $\Delta v_{\mathrm{chan},i}$ the width of channel i (Teague 2019). It is also possible to calculate a moment uncertainty, but we neglect this in favor of the method presented in section 2.3.1.

These moments can be calculated on all the spectra in a data cube to create a moment map. However, creating such a moment map is not necessarily a trivial process. This is because the moments cannot simply be calculated with the spectra as they are—the noisy regions would deteriorate the quality of such a map, especially for higher-order moments. Rather, a mask must be created to isolate only the emitting regions of the data cube. One way to do this is to apply a σ mask, where everything below a certain noise threshold is masked out during the moment calculation. This is a good first attempt, but it often misses flux and makes the maps somewhat messy. A better method, while tedious, is to manually mask each slice of the data cube with a (large-vertex number) polygon region.

We created these masks using a proprietary code created in the Interactive Data Language (IDL). Before masking, the data cube was trimmed in all three dimensions, leaving a buffer of at least 5 channels on each side of the detected CO emission to ensure a background noise level can be measured. Manually-input polygon vertices were then used to define the emission region within each channel. Since the nature of interferometry tends to leave a negative bowl around the emission, we reject any negative values from each spectrum as a redundancy to account for human error when masking. After masking, we calculated initial zeroth, first, and second moments for each spectrum according to equations 2.1, 2.2, and 2.3, respectively, then collected these into spatial maps for inspection.

Each flux map was binned using a Voronoi tessellation to compensate for lower S/N with increasing distance from the disk center by combining together adjacent spectra (Cappellari & Copin 2003). The target S/N for the binning routine was chosen so as to roughly bin the central 1–2 beam width regions at the pixel scale, with bin size increasing at higher radii. This resulted in a typical target S/N of about 5, though in some barely-resolved cases we were able to go down to 3 and still recover high-quality moment maps. After combining the spectra within each bin, we recalculated the moments and collected them into binned moment maps.

While Voronoi tessellation does improve the S/N properties of the data, it has the unfortunate side effect of binning individual spectra to uneven spatial dimensions. This presents a problem when analyzing the disk kinematics, since any elliptical extraction from the moment 1 map will recover blockily-averaged kinematics. To assuage this problem, we interpolate our Voronoi-binned maps down to the pixel level using the bin centroids and the "thin plate spline" radial basis function (Duchon 1977) available in the SCIPY library (Virtanen et al. 2020). This method of interpolation was chosen because it sufficiently retains small-scale features without introducing substantial noise (i.e., it minimizes residuals when compared with the unbinned moment map). We restrict the interpolation to points contained within the Löwner-John ellipse defined by the Voronoi bin centroids (John 2014), as we found that any extrapolation consistently produced unreasonable kinematic features. Before interpolating, we also throw out any obviously bad bins, as well as those with relatively low S/N.

Moment Uncertainties

There are 2 main sources of uncertainty in our data. For moment 0 maps, the $\sim 10\%$ uncertainty from flux amplitude calibration dominates (Fomalont et al. 2014). For moment 1 and 2 maps, the flux uncertainty has little to no effect since it only scales the entire spectrum up or down. Instead, the uncertainty due to noise dominates. Unfortunately, the calculation of such a statistical uncertainty for interferometric data is not as straightforward as for photometric data; the observation and deconvolution process does not allow us to make the assumption that each spectrum is independently sampled from those adjacent to it. Therefore, instead of attempting to describe it analytically (e.g., per Teague 2019), we recover the uncertainty in each spectrum after the fact via a Monte Carlo resampling process.

To do so, we first assume that each datum in each binned spectrum was sampled from a 2D Gaussian prior distribution in flux and velocity space. In the flux direction, we assume a width

equivalent to the standard deviation of the line-free region of the spectrum. In the velocity direction, we assume a standard deviation of 10% the velocity channel width. Each binned spectrum is "resampled" by randomly generating a new spectrum from the prior distributions, after which the moments are recalculated. This is repeated ~ 100 times, and the standard deviation of these is then taken as the moment uncertainty for that spectrum. The uncertainties tend to be higher for all three moments at $r \lesssim \theta_{\rm FWHM}$ (due to wider spectra from beam smearing), as well as large r (due to higher noise). An example (for galaxy NGC 383) of each raw moment, binned moment, and moment uncertainty map is given in Fig. 2.1.

2.3.2 KINEMETRY

To quantify the kinematic properties of the galaxies, we make use of the KINEMETRY code by Krajnović et al. (2006), which is a generalization of photometry to higher order moments of the line-of-sight velocity distribution. In general, it performs a harmonic decomposition of the moment map along ellipses of increasing radii. In this case, we apply the decomposition to the first moment (line-of-sight velocity). Because the gas velocity field is expected to be in mostly circular rotation about the center, the coefficient k_1 (i.e., the quadrature sum of the coefficients for the $\sin\phi$ and $\cos\phi$ terms) quantifies the amplitude of the bulk rotation of the disk. As the Fourier coefficients are fit, KINEMETRY simultaneously fits the position angle (Γ), or the angle of maximum velocity, and flattening (q) at a given radius. Flattening is related to disk inclination (i) at a given radius with $q = \cos i$, where $i = 0$ corresponds to a face-on distribution. Note that this is only true for infinite resolution, however, and beam smearing effects tend to artificially drive q towards 1. Changes in both Γ and q as a function of radius quantify disk warping. We also make use of the ratio of the higher-order k_5 coefficient to k_1, which quantifies deviation from circular rotation (e.g., due to gas inflows/outflows). The coefficients k_2 and k_4 are not used due to being unphysical, and neither is k_3 because it is minimized as Γ and q are minimized.

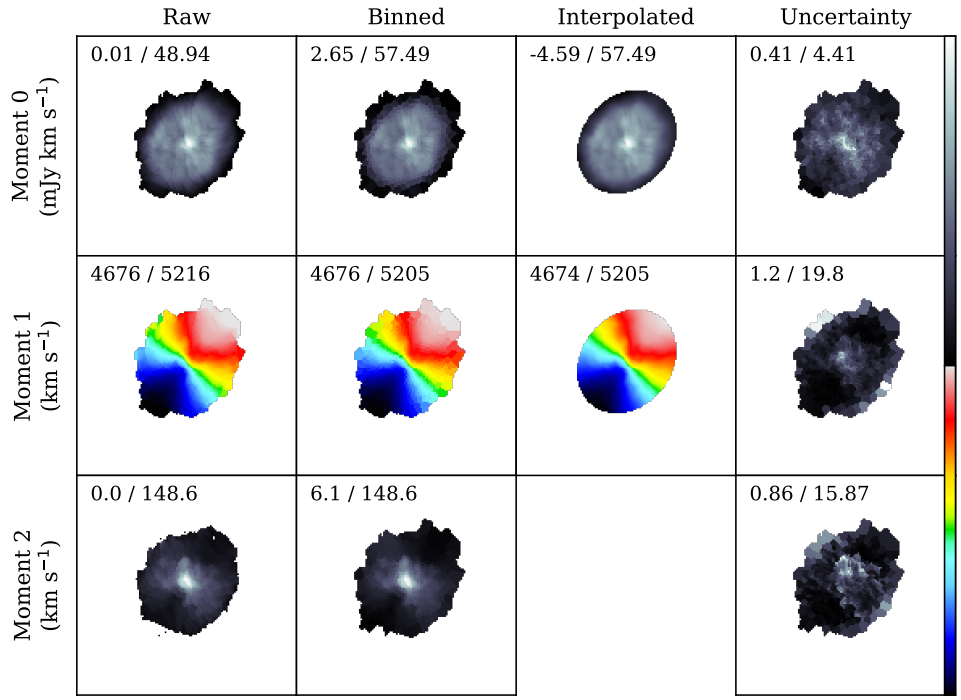

Figure 2.1 The first three moments of NGC 383 (data taken from ALMA project 2015.1.00419.S). The first column is the raw moment calculated at each pixel after manual masking. The second column is the Voronoi-binned moment. The third column is the interpolated (thin-plate spline) moment which was passed to KINEMETRY, as detailed in section 2.3.1. The fourth column is the moment uncertainty per section 2.3.1. Colorbars are shown on the right which correspond to the lower/upper limits shown in each map (with units given on the left).

Parameter Tuning

There are some input parameters to which KINEMETRY is quite sensitive. To ensure the use of ideal parameters without introducing extra uncertainty, we fit the representative case of NGC 1332 multiple times while varying the most impactful parameters. Specifically, we vary: "drad" (the size increase in pixel units of each successive ellipse); "cover" (the fraction of the ellipse with data points required for KINEMETRY to continue); "npa" and "nq" (the resolution of the grid from which Γ and

q are fit, respectively); and the extrapolation distance, discussed earlier. While each parameter was varied, everything else was kept at a conservative value (e.g., high sampling, high cover fraction, etc.) to isolate the effect of just one parameter.

Importantly, we find that the fit is not overly affected by the fineness of sampling in Γ and q. We therefore decide to keep "npa" and "nq" at 40 for the entire sample as a good balance between computational speed and accuracy. Varying the "drad" parameter also does not change the KINEMETRY fit significantly, so, for uniformity's sake, we adjust the parameter to aim to fit 20–30 ellipses for each target (as long as "drad" does not have to be decreased below 1 pixel, as adjacent Γ, q, and k_1 values would be redundant). The cover fraction does not affect the KINEMETRY fit at all interior to a certain radius, since the cover fraction is nearly always 1, but it might allow the fit to extend to slightly larger radii. Below a certain cover fraction, the results do start to become unreasonable, with large, unexpected swings in Γ, q, and k_1. For each target, we therefore decrease the cover fraction as low as possible as long as these parameters remain smooth.

2.4 Molecular Gas Properties

We also employ the moment 0 maps from our sample to quantify the molecular gas properties. A total intensity ($I_{\rm CO}$) is calculated by integrating the entire binned moment 0 map. The total emission-line luminosity ($L'_{\rm CO}$) is then found with

$$L'_{\rm CO} = 3.25\times10^7 S_{\rm CO}\Delta v \frac{D_L^2}{(1+z)^3\nu_{\rm obs}^2}\ {\rm K\ km\ s^{-1}\ pc^2}, \tag{2.4}$$

where $S_{\rm CO}\Delta v$ is the line intensity (Boizelle et al. 2017; Carilli & Walter 2013). We then convert this to a CO(1−0)luminosity with $I_{\rm CO(2-1)}/I_{\rm CO(1-0)} \approx 0.70$ and $I_{\rm CO(3-2)}/I_{\rm CO(1-0)} \approx 0.49$, and a molecular hydrogen mass is found with $M_{\rm H_2} = \alpha_{\rm CO} L'_{\rm CO}$ where $\alpha_{\rm CO} = 3.1\ M_\odot\ {\rm pc^{-2}}\ ({\rm K\ km\ s^{-1}})^{-1}$ (Sandstrom et al. 2013). Finally, this is converted to a total gas mass assuming $M_{\rm gas} = (1+f_{\rm He})M_{\rm H_2}$

where $f_{\rm He} = 0.36$ is the helium mass fraction (Boizelle et al. 2017). Values of $I_{\rm CO}$, $L'_{\rm CO}$, and $M_{\rm gas}$ for each galaxy in our sample can be found in table B.1.

2.5 Dust Continuum Properties

In order to get a fuller picture of the CNDs in our sample, we also look at the dust properties. While dust is a relatively minor component of the disk mass-wise, it can be used to constrain the temperature and mass of the CND as a whole. Additionally, dust gives insights into the CND's origin, lifetime, etc. (see section 1.1.2). While fitting the IR continuum of an ETG has been used in the past to study CND dust, this method has often suffered from sparse wavelength sampling and coverage, as well as poorly constrained fits. Due to the self-absorptive nature of the dust, it is typically modeled as a "modified" blackbody which directly accounts for emissivity. That is,

$$S_\nu = \frac{\kappa_\nu M_{\rm dust} B(\nu, T_{\rm dust})}{D^2}, \tag{2.5}$$

where S_ν is the flux density, $M_{\rm dust}$ is the dust mass, D is the luminosity distance, $B(\nu, T_{\rm dust})$ is the Planck function with dust temperature $T_{\rm dust}$, and κ_ν is the dust absorption coefficient. This is related to the dust emissivity with $\kappa_\nu \propto \nu^\beta$, where β is the dust emissivity index (Davis et al. 2017). In this work, we adopt an empirical $\kappa_0 = 1.92$ cm^2 g^{-1} for $\nu_0 = 856.6$ GHz (Draine 2003), but allow β to vary during the fitting process.

Unfortunately, when β is allowed to be a free parameter, the modified blackbody fit is especially difficult to constrain on the Rayleigh-Jeans (red) tail. The ALMA continuum data described in section 2.2 solves this problem in some cases. In this section, I describe the process of obtaining archival photometric data from multiple observatories across the IR spectrum to fill out the spectral energy distribution (SED) for each target. I then detail how this is used in tandem with ALMA continuum data to fit a modified blackbody to the data and constrain the dust temperature, mass, and emissivity.

2.5.1 IR Flux Data

The NASA/IPAC Extragalactic Database (NED) serves as an archive of flux density measurements from the literature for extragalactic objects. Not all the IR measurements therein suit our purposes well, since they were made at a variety of sensitivities, resolutions, aperture sizes, wavelengths, etc. Most of the mid to far-IR measurements in NED were made from observations unable to resolve the CND. Fortunately, we expect most, if not all, of the galaxy-integrated continuum mid-IR emission to arise from the CND. Therefore, to measure total dust brightness, we prefer measurements that were integrated over the entire galaxy, but which are still resolved enough to separate any significant contaminating sources. For each target, then, we use only NED values from the IRAS Faint Source Catalog (FSC; Moshir 1990), as well as the ISO and Spitzer observatories as long as they were integrated over a sufficiently large radius. In the few cases where targets are not included in the IRAS FSC, we use IRAS 100 and 60 μm measurements from Knapp et al. (1989).

In some galaxies, synchrotron emission from an AGN also dominates at longer wavelengths and can affect the shape of the Rayleigh-Jeans tail. With this in mind, we also take radio measurements from NED as long as they were integrated over the entire galaxy. Specifically, we use data from the following observatories: the Australia Telescope Compact Array (ATCA; Ghosh et al. 2005; Murphy et al. 2010), the Parkes Observatory (Disney & Wall 1977), the Effelsberg 100-m Radio Telescope (Vollmer et al. 2004), the Molonglo Observatory Synthesis Telescope (Mauch et al. 2003), the Arecibo Telescope (Dressel & Condon 1978), and the Very Large Array (VLA; Baan & Klöckner 2006; Brown et al. 2011; 2017; Condon et al. 2002; Cox & Sparke 2004; Leipski et al. 2006; Mundell et al. 2009; Nagar et al. 2005).

New Photometric Measurements

While NED hosts a large number of useful flux density measurements, it is not comprehensive, nor are some of the measurements necessarily suited for our purposes here. For example, it is hard to

find WISE or Spitzer (IRAC instrument) flux densities which were integrated over a sufficiently large aperture. Also, some targets have archival images, but with no flux density measurement in the literature, so none exists on NED.

This is primarily the case with the Herschel Space Observatory, which observed at 500, 350, and 250 microns (SPIRE instrument), as well as at 160, 100, and 70 microns (PACS instrument). Many of the targets from our sample did not have flux densities measured in point or extended source catalogs because they are very faint or contaminated by background sources due to the low angular resolution at longer wavelengths. Nevertheless, these longer wavelength observations can prove critical in constraining the shape of the continuum emission, so we do the aperture photometry ourselves to obtain new flux density measurements. This is done by first gathering the Herschel High Level Image (HHLI) mosaics from the NASA/IPAC Infrared Science Archive (IRSA). The targets are then integrated over an aperture which gathers all visible emission from the galaxy while avoiding any obvious contaminating sources. This corresponds to roughly 2–3 times the effective (or half-light) radius of the stellar distribution at optical wavelengths in most cases. After integrating, we obtained absolute PACS flux densities by applying color corrections of 0.977, 0.974, and 1.037 for the 70, 100, and 160 μm bands, respectively (assuming the mid to far-IR intensity is dominated by a modified blackbody at 30 K with $\beta = 2$; Müller et al. 2011). For the SPIRE flux densities, the color corrections are 0.9881, 0.9757, and 0.9853 with pixelation corrections of 0.997, 0.993, and 0.902 for the 250, 350, and 500 μm bands (also for $\beta = 2$; Valtchanov 2018). For all Herschel flux densities, we calculated a statistical uncertainty by repeatedly (and randomly) shifting the aperture to nearby, source-free areas, reintegrating, and taking the standard deviation of these test measurements. A systematic uncertainty of 7% for PACS (Exter 2017) and 10% for SPIRE (Valtchanov 2017) was also assumed, and these were then combined to estimate a total flux density uncertainty.

We also explore the near to mid-IR SED behavior by retrieving high-level science images from IRSA for the WISE W1, W2, W3, and W4 bands (3.368, 4.618, 12.082, and 22.194 μm respectively), as well as the Spitzer Infrared Array Camera (IRAC) 1 and 2 bands (3.551 and 4.493 μm, respectively). We measured total flux densities for each target in each band using the same method described for the Herschel data. The only exception was that the statistical uncertainty was found from the RMS flux density of a source-free ten-by-ten pixel square, since the apertures are often too big to find a sufficiently large source-free region. For the WISE values, we applied a standard flux density conversion assuming a color correction for a K2V source that is characteristic of the stellar populations of old and red ETGs (Cutri et al. 2012). For the Spitzer values, we applied color corrections listed in the IRAC Instrument Handbook (IRAC Instrument and Instrument Support Teams 2021), again assuming $\beta = 2$ for the stellar light. Additionally, we applied the recommended aperture corrections as a function of effective circular radius. As with all other flux data here, the final error budgets are dominated by the uncertainties in the absolute flux standardization of each filter. We adopted systematic uncertainties of 2.4, 2.8, 4.5, and 5.7% for bands W1, W2, W3, and W4, respectively; for Spitzer flux densities, we assume absolute uncertainties of 10% for extended sources per the IRAC Instrument Handbook.

2.5.2 SED Fitting

After measuring additional continuum flux densities, the SEDs typically have at least 3 points over the mid to far-IR range to anchor a modified blackbody fit. Exceptions are NGC 3258, and NGC 3268, which have only two non-ALMA points, as well as NGC 997 that has one IRAS measurement and one ALMA flux density. Before fitting the mid to far-IR points, we first subtract any contamination from AGN synchrotron emission. To do this, we fit the radio points—along with the unresolved ALMA continuum flux density as described in section 2.2—with a power law. This power law is then subtracted from all other far-IR points in the SED. At the same time, we also fit a

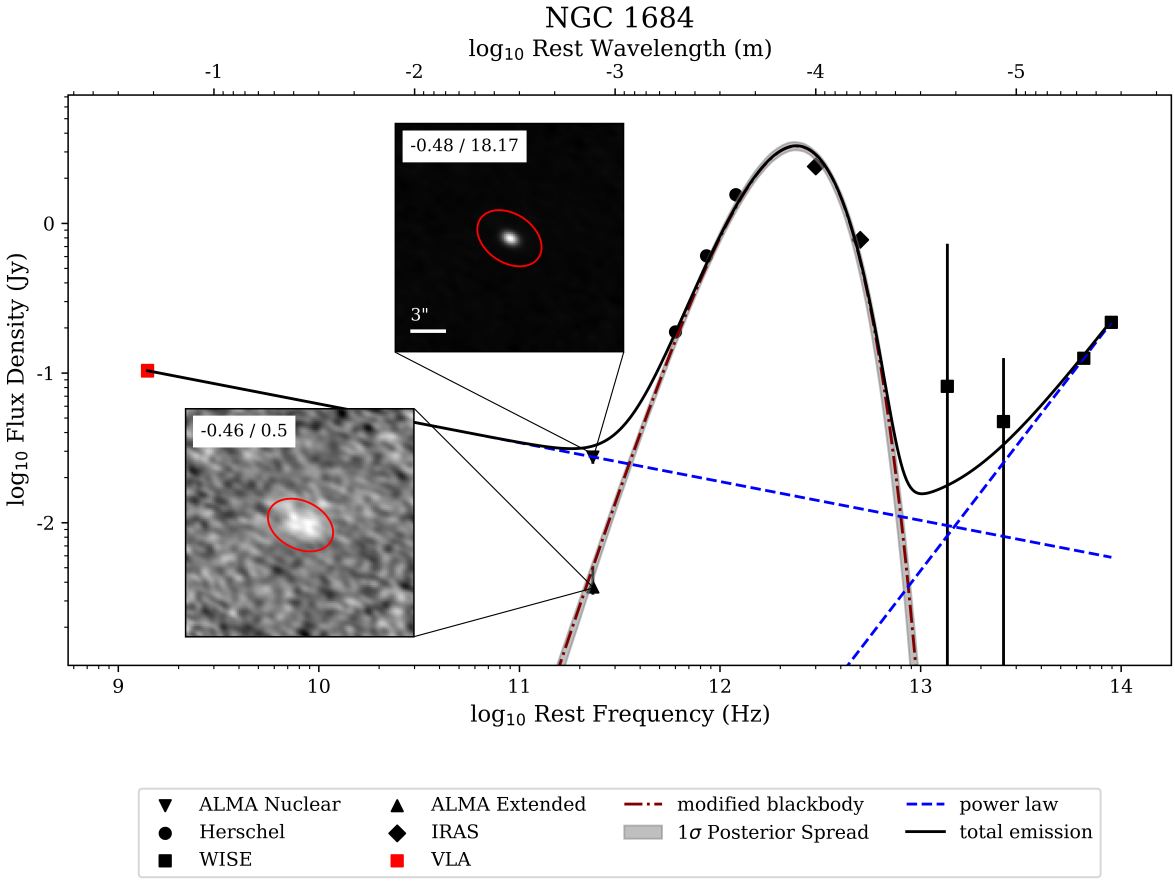

Figure 2.2 SED for NGC 1684. Blue dashed lines show fitted power laws for AGN emission (left) and stellar emission (right). The top ALMA image is the total continuum (used for the radio power law fit), while the bottom is the point-source subtracted continuum used for the modified blackbody fit; red ellipses show the integration region used to determine the flux density, and min/max values for the image (mJy/beam) are shown in the upper left. The red dot-dashed line and the gray filled line shows the modified blackbody fit and the 1-σ posterior distribution from MCMC, respectively. This fit has a temperature of 22.50 ± 1.08 K, a mass of $2.851 \pm 0.479 \times 10^7\ M_\odot$, and $\beta = 2.158 \pm 0.145$.

power law to the stellar emission in the near IR with WISE W1 and W2, and IRAC 1 and 2 bands. This stellar continuum fit is not subtracted, though, since in every case it is at a significantly lower level than the thermal dust continuum, but we still include it for reference.

After subtracting contamination, we fit a modified blackbody to the Herschel (SPIRE and PACS), IRAS (60 and 100 micron), ISO, and Spitzer (MIPS) points, as well as the point source-subtracted ALMA continuum image as described in section 2.2. The modified blackbody used is that described in Davis & Bureau (2016), and we use MPFIT, a least-squares fitting routine developed by Markwardt (2009). Additionally, we perform the fit using Markov chain Monte Carlo (MCMC) with EMCEE (Foreman-Mackey et al. 2013). MCMC refits the model several thousand times with slightly different parameters to explore the model cost at different locations in parameter space, followed by finding best fit values at the parameter-space minimum. One advantage to this is that we better understand the parameter uncertainties, as we can see how the model cost changes accordingly. Also, correlations can be seen between the fitted parameeters. See Fig. 2.3 for an example of this from the modified blackbody fit of NGC 1684.

After fitting, we also use a Monte Carlo resampling technique to better understand the parameter uncertainties. To do this, each flux density datum is resampled 100 times from a normal prior distribution with a width corresponding to its statistical uncertainty. At each of the 100 iterations, the modified blackbody is refit, and the standard deviation of the refitted parameters are taken as the uncertainties. A summary of fitted dust properties and uncertainties for each target can be found in the appendix, along with SEDs with 1-σ posterior distributions from MCMC for reference.

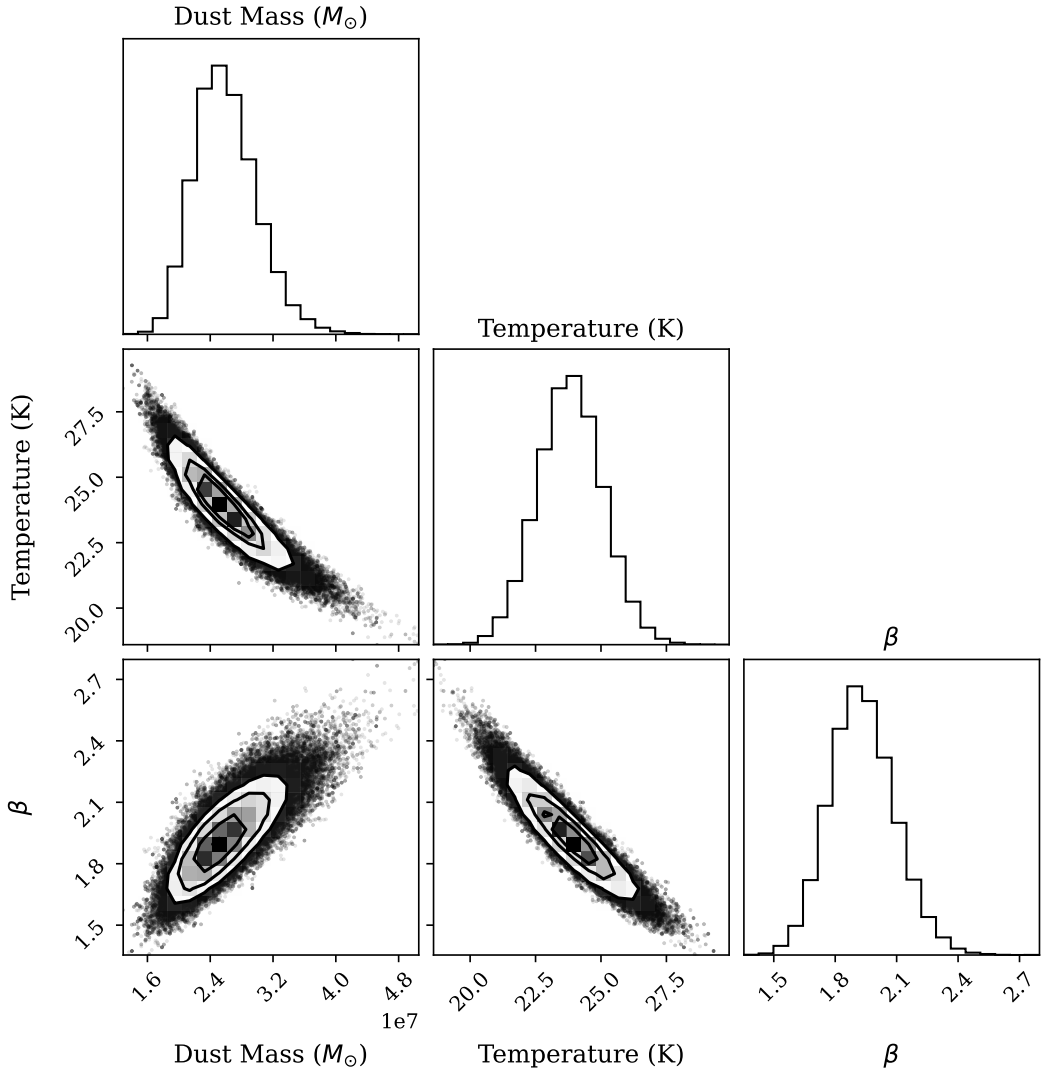

Figure 2.3 EMCEE results for the modified blackbody fit shown in Fig. 2.2. Each histogram shows the posterior distribution of that parameter, with higher density indicating a greater likelihood of the true parameter being found there. The scatter plots show the shape of the parameter space in the two corresponding parameters. Note the sloppiness (elongation) of all the parameter combinations, which signifies that there is some degeneracy between all the parameters.

Chapter 3

Results and Discussion

With dust properties and gas kinematics measured for our sample, we now turn to its analysis. While the bulk of this work has already been presented, a few things remain to be discussed. First of all, in this chapter, I present an analysis of how reliable the data is and how well it returns the intrinsic properties of the CNDs. I also look at some preliminary statistics of our sample to confirm it matches other ETG surveys, as well as discuss what can be learned from our sample that might not be able to be learned from other surveys. Finally, I present some conclusions about what can be learned from our data, and discuss further avenues for research.

3.1 Reliability

One important question is how well the data here represent reality. For example, central holes in the CO distribution are well resolved in some cases, but may simply be undetected in other cases due to spatial blurring of the data. This is an example of the effect of finite angular resolution and seeing conditions on our observations. In general, there are three main reasons why our data might be misleading: finite angular resolution, as demonstrated; finite sensitivity; and measurement uncertainty.

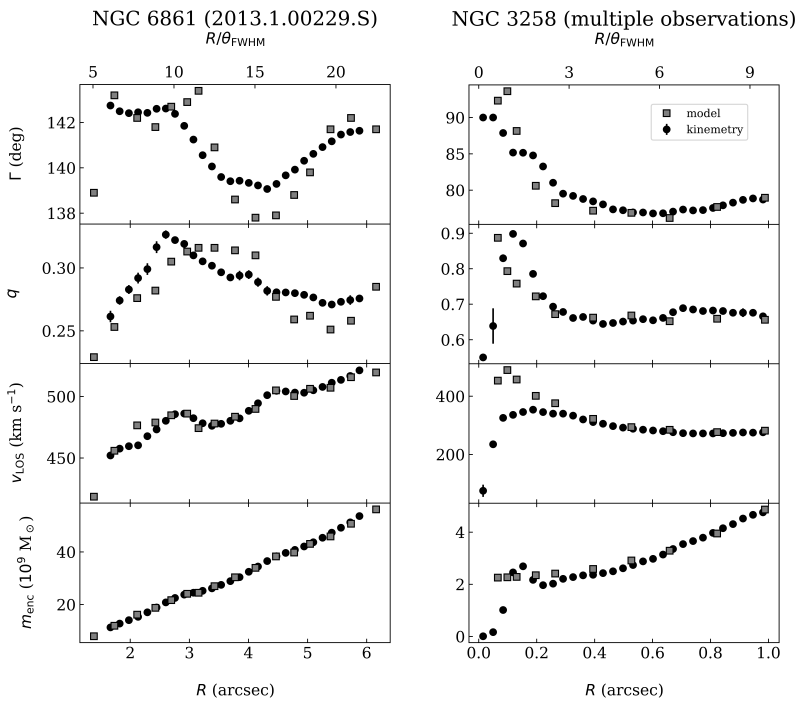

Figure 3.1 Representative KINEMETRY results compared to intrinsic tilted-ring parameters from gas dynamical models. The top scale shows the number of beam widths corresponding to the sky scale on the bottom. When the beam is small relative to the disk extent (e.g., NGC 6861), they agree well. However, KINEMETRY diverges from the true kinematics below about 3 beam widths from the center. Note the Keplerian velocity upturn in NGC 3258 that is barely detected by KINEMETRY.

Let us first address the problem of angular resolution. ALMA observations typically can achieve beam sizes on the order of 0.1–0.5″. This typically means the ability to resolve CND features on scales of ∼100 pc for local ($D_L \sim$ 20–40 Mpc) galaxies. Despite this incredible resolving power, CNDs often contain interesting features smaller than this limit, such as distinct gas clouds or central holes. Disk warping and turbulence also tend to increase in the central region due to being closer to the central SMBH.

This means that small-scale features (especially close to the SMBH) remain undetectable in these observations. Rather, there is a "beam-smearing" effect where the features are blurred together with neighboring gas. For example, a position angle twist or a change in disk inclination will tend

to be less exaggerated and occur at a larger radius. Similarly, whereas an observation with perfect resolution would always show an increase in k_1 towards the center inside the SMBH sphere of influence, a lower-resolution observation smears together blue and redshifted emission and might erase a rise in k_1 altogether. These effects can be seen illustrated in Fig. 3.1, where the KINEMETRY results for two sample observations are compared to gas dynamical models. The tilted-ring model illustrated there is outside the scope of this work; suffice it to say that it comprises fitting annuli at a range of radii with different Γ and q solutions to the data along with a few physical parameters including the SMBH mass, gas turbulence, etc.

ALMA observations do have better sensitivity limits than previous surveys, but still not all emission from the CND is detected. When using radio interferometry, there is inherently a tradeoff between high sensitivity and high angular resolution. While on one hand the antennas can be placed further apart to better the angular resolution (analogous to how a larger aperture on an optical telescope supplies better resolution), this comes at the cost of lots of short baselines, which are better at detecting total power from a target. Figure 3.2 shows two observations of NGC 315 to illustrate this point. In practice, data from multiple observations such as these can be combined to yield high resolution and sensitivity, but the process is often tedious and painstaking.

As discussed earlier, there is also a 10% flux uncertainty in all ALMA observations due to flux calibration using slightly variable quasars (Fomalont et al. 2014). This must be factored in when using the moment 0 map to make any inferences about gas properties. This does not affect velocity maps, however, since a flux uncertainty offsets the entire line-of-sight velocity distribution in the same direction.

When taking all of these observational effects into account, a few conclusions can be made about what can and cannot be learned from the data. First of all, as mentioned, all inferences from moment 0 data should have the flux uncertainty factored in. It should also be remembered that we may not necessarily be seeing the whole disk, so our estimates of gas mass or other similar

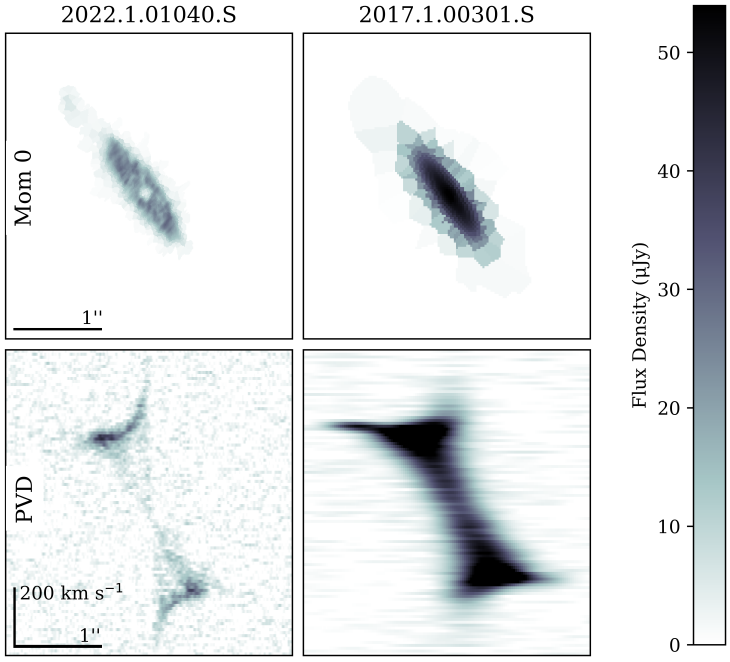

Figure 3.2 Top: Voronoi-binned CO moment 0 maps from two different observations of NGC 315 at the same scale and orientation, but at very different angular resolutions and sensitivities. Notice that the right observation is more sensitive to larger-scale, smoother emission, but the left one is able to detect finer features, such as a central hole. Bottom: Corresponding PVDs for the images shown on top. Note the Keplerian velocity upturn clearly detected in the left observation but significantly blurred out in the right observation.

properties may be lower bounds. Similarly, small-scale features may not be detected, and it is hard to make any conclusions such as what fraction of our sample has a central hole, central warping, etc. (though, again, a lower limit could be placed). On the other hand, moment 1 maps are significantly less misleading, except at small radii (specifically, less than $\sim$3 beam widths; see Fig. 3.1). The general kinematic structure can be trusted, which was also seen in section 2.3 where we found that KINEMETRY is not extremely sensitive to input parameters.

3.2 Sample Properties and Statistics

Now I explore whether our sample as a whole tends to agree with results obtained by other ETG surveys. As described in section 1.1.2, the formation and retention mechanisms for CNDs are hotly debated, and looking at the kinematics, masses, and warping of a large number of CNDs can help answer these questions. I will first look at the misalignment between the CND and the galaxy's stellar component, and compare that with ATLAS^{3D}. I then also examine the distribution of dust masses in our sample, how these relate to the gas masses, and how both of these correlate with the extent of the CND. It is important to keep in mind here that while the sample is not completely unbiased (i.e., CNDs were selected for being regular in shape and easy to see due to highly opaque dust), it is representative of nearby, regularly rotating CNDs in ETGs.

3.2.1 Kinematic Misalignment

Krajnović et al. (2011) use SAURON data to make stellar velocity maps and then measure the average kinematic position angle. These are then compared to the gas kinematic position angles obtained in a similar manner. Unfortunately, due to a portion of our sample being located in the southern hemisphere, we lack such data to make stellar velocity maps for all targets. Instead, to maintain uniformity, we measure stellar photometric position angles at optical wavelengths. While not ideal, the stellar photometric axes are, in most cases, well-aligned with the kinematic axes.

This is done using the `find_galaxy` routine of the MGEFIT package (Cappellari 2002). We apply this to WISE W1 band images to find the image moments of the target (out to 2.5 half-light radii), which are then used to find the position angle. The difference is found between this and the median position angle from KINEMETRY to get the misalignment angles shown in Fig. 3.3.

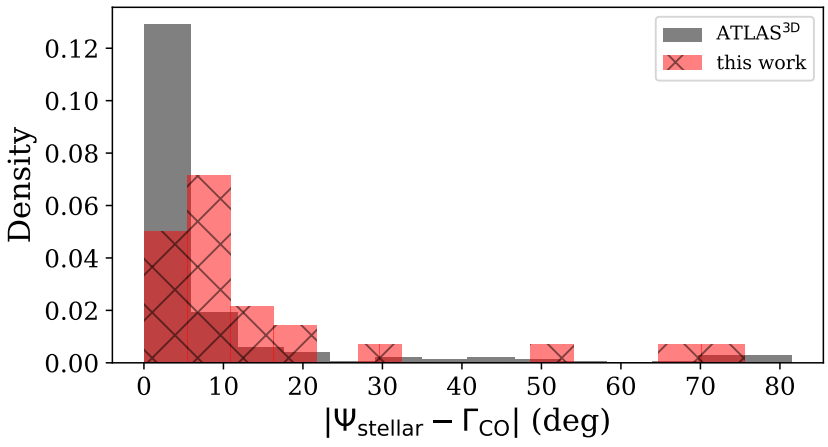

Figure 3.3 Stellar/CND misalignment angles from this work (red hatched) shown against the ATLAS^{3D} misalignment angles (gray dotted; Krajnović et al. 2011).

3.2.2 Total Dust/Gas Mass and Extent

Since dust mass and gas mass are expected to be tightly correlated, an important check is provided by comparing the two from our current sample. This is shown in Fig. 3.4. As can be seen, there is a moderately tight correlation between gas and dust mass, as expected. A power-law fit to our sample yields a gas-to-dust mass ratio of 98, consistent with the generally-assumed 100 shown in the figure (Sandstrom et al. 2013). This gives us confidence in both the dust and gas mass measurements, since they are done completely independently, with the dust mass being supported by other IR data besides ALMA.

Additionally, as detailed in chapter 1, it is not well known where the gas and dust in CNDs comes from originally. Interestingly, as can be seen in Fig. 3.5, there is a correlation between disk extent and gas surface mass density. This implies that whatever the formation mechanism, the gas reservoir has a similar capacity regardless of final CND size.

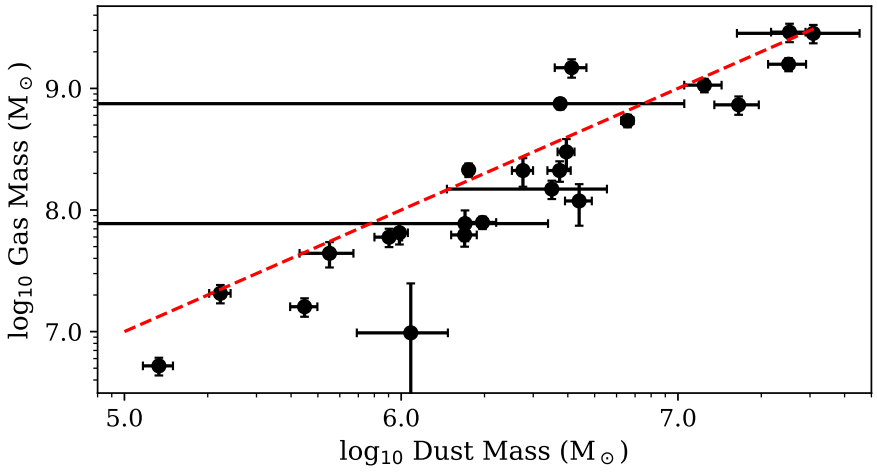

Figure 3.4 CND gas versus dust mass for all galaxies in our sample except those that could not be fit due to a lack of SED data. The dashed line gives the 100:1 ratio for gas to dust mass, along which our data lie nicely.

3.3 Conclusions

Regular CNDs in ETGs are a key component in piecing together the picture of galaxy evolution in general, and here we have made some progress towards this goal. Since the turn of the century, multiple large-scale ETG surveys have laid the groundwork for understanding the dust and gas properties of CNDs. While these have helped astronomers generally get a grasp of CND composition and kinematics—as well as occurrence rates, sizes, and generally how they interact with a host galaxy—such surveys have also been limited by resolution and sensitivity constraints. Recent ALMA observations have allowed for highly sensitive, resolved images of CNDs. On one hand, continuum images from ALMA are vital in fitting the Rayleigh-Jeans slope of the thermal dust emission, thus allowing for more tightly constrained measurements of dust temperature, mass, and

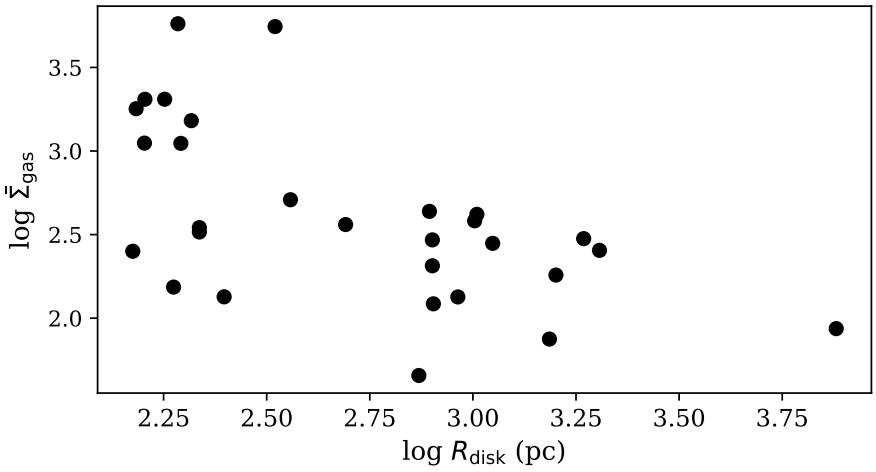

Figure 3.5 Gas surface mass density versus CND radius for all galaxies in our sample.

emissivity. On the other hand, spatially-resolved spectral-line observations allow us to map both the surface brightness and kinematics of the molecular gas in CNDs.

Despite the quantity (greater than 100) of such high-quality observations in the ALMA archive, many of these have previously remained underutilized for the purpose of getting a statistical picture of CNDs in ETGs. Here we have presented the beginnings of such a survey; this will both complement previous ETG surveys by looking at new targets, and further our knowledge of CND gas and dust properties due to the unparalleled resolution of ALMA images. To make this more doable, we have limited ourselves here to only those galaxies observed through cycle 3 (see section 2.1 for details on sample selection).

While much of the work presented here is still in a preliminary form, there are some general conclusions that can be made. First of all, we made a point here to refine our use of KINEMETRY

so that it can be applied uniformly to a large number of observations. One concern was that KINEMETRY might be unreasonably sensitive to input parameters such as noise in the data, fitting resolution, etc. Fortunately, we found that this is not the case, and that—given a reasonably resolved velocity map—the same results are generally obtained regardless of fine tuning of input parameters. At the very least, then, this implies that the kinematic properties recovered from KINEMETRY are consistent.

Nevertheless, this does not necessarily say anything about the accuracy of the KINEMETRY results. To get a better understanding of how much these represent physical reality, we compared them to full gas dynamical models. We found that, in general, there is significant beam smearing below about 3 beam widths, so such small-scale data cannot be completely trusted. Still, general trends in position angle or flattening change can be seen—they are just smeared out to larger radii. Also, above about 3 beam widths, the KINEMETRY results match the gas dynamical models very closely. As with any data, ALMA also suffers from finite sensitivity which generally gets worse in observing configurations which offer better angular resolution. As such, continuum or gas surface brightness maps should also be taken with a grain of salt, though this is probably within the 10% absolute flux calibration uncertainty.

In this work we have also presented SEDs for our sample, with IR data gathered from multiple other observatories. In general, the ALMA continuum data has given the expected results: provided a better fit to the modified blackbody, with the Rayleigh-Jeans slopes matching both the literature and Herschel data, where present. In a few cases, the ALMA flux density measurement lies significantly above what would be expected given the rest of the data for that target. This is probably due to contamination from other unaccounted-for sources, such as bright radio jets. An effort has been made to mask these features where possible, but has not been perfect. Regardless, in these cases, the other mid to far-IR data does a good job at constraining the fit, and we are confident that the blackbody-fitting methods discussed in this paper will apply well to a larger sample and give

generally consistent results. The dust and gas masses from our sample have been cross-checked with each other to show that their ratio is at least consistent with the literature, giving us more confidence that the modified blackbody fit does a good job at recovering dust properties.

Results from dust fitting and gas kinematics have been combined to make some preliminary conclusions—and consistency checks with the literature—about our sample. First of all, we find that, as in Krajnović et al. (2011), the gas kinematics are generally aligned with the galaxy's stellar component. There is still a significant misalignment measured in some fraction of the sample, but a lot of these are more circular, so it is harder to measure a position angle. Additionally, since we lack stellar kinematic data for our sample, we are comparing gas kinematics to the stellar photometric axes. This differs from ATLAS^{3D}, which compares the kinematics of both. Nevertheless, this should be explored further, and the sample will become more statistically significant as more galaxies are added. Finally, we also find a correlation between the physical extent of a CND and the gas surface mass density (Fig. 3.5). This implies that a larger disk has a smaller gas density.

3.4 Moving Forward

At this point, we turn to applying what has been learned here to all the CNDs present in the ALMA archive. While we have generally confirmed the results from other ETG surveys—stellar/gas kinematic alignment, kinematic warping, gas to dust mass ratio, etc.—many questions remain to be answered. Adding more targets to our sample will help get a more accurate statistical picture of these things and CNDs in general.

One question, for example, which will be further illuminated with a larger sample is the occurrence rate of holes and other central features in these gas disks. Some CNDs, such as NGC 6861, are seen to have a large central hole in the gas distribution. We expect these to occur relatively frequently, but there are too few such detections in our current sample or previous ETG surveys to

say with any certainty. The high angular resolution of observations yet to be included in our sample will make a more detailed study possible. In general, more targets will allow us to get a better look at the surface brightness profiles for a large number of galaxies. For example, among the galaxies presented here, most have monotonically decreasing surface brightness profiles, but there are quite a few exceptions with large central holes, multiple rings, etc. Also, Davis et al. (2013) find that the molecular gas surface brightness profiles follow the stellar distribution in approximately half of all ETGs, with a third having molecular gas distributions that fall off slower than the stellar profile. Exploring this will help determine the recency of merger or accretion events in the sample.

Some observations presented herein have good enough resolution to detect a central rise in velocity due gravitational interaction with the central SMBH. In such cases, it may also be possible to measure the mass of the SMBH by fitting the velocity profile (e.g., as done in Boizelle et al. 2019). Further work on the rest of the ALMA archive will inevitably identify many more targets for such study. An increasing number of SMBH mass measurements in ETGs with CNDs will add another data point in our quest to understand how CNDs interact with their host galaxies.

As we move forward with gathering CND kinematics, gas distributions, dust properties, and other data such as SMBH masses, we continue to piece together a fuller picture of CND formation and retention. While lots of questions still need to be answered, this is a good start to better understand galaxy evolution as a whole and why the ISM in any galaxy has the morphology it does.

Appendix A

New Flux Density Measurements

Table A.1. New Flux Density Measurements

Galaxy	ALMA Band	ALMA Continuum Nuclear (mJy)	ALMA Continuum Extended (mJy)	SPIRE 500 μm (Jy)	SPIRE 350 μm (Jy)	SPIRE 250 μm (Jy)	PACS 160 μm (Jy)	PACS 100 μm (Jy)	PACS 70 μm (Jy)
NGC 0383	6	81.6	11.9 (1.5)	0.11	0.334	0.784	1.41	1.21	···
NGC 0524	6	16.4	3.34	···	···	···	···	···	···
NGC 0708	6	4.38	<0.0578	···	···	···	···	···	···
NGC 0997	6	9.49	2.72	···	···	···	···	···	···
NGC 1332	6	8.97	1.14	···	···	···	···	···	···
NGC 1380	···	···	···	0.0812	0.325	1.02	2.2	2.84	···
NGC 1386	3	6.01	1.21	0.467	1.44	3.62	8.42	8.74	6.53
NGC 1387	3	2.14	0.792 (0.16)	0.312	1.02	2.59	6.03	6.76	···
NGC 1684	6	29.5	5.72 ($^{+2.3}_{-0.6}$)	0.188	0.607	1.55	···	···	···
NGC 3258	···	···	···	···	···	···	···	···	···
NGC 3268	···	···	···	···	···	···	···	···	···
NGC 3557	6	27.3	1.55 (0.18)	···	0.0604	0.11	···	···	···
NGC 3607	6	4.41 (0.48)	0.155 (0.26)	0.123	0.556	1.24	3.28	···	1.87
NGC 3862	6	114	14.6	···	···	···	···	···	···
NGC 4061	6	4.95 (0.58)	3.16 (0.56)	···	0.0974	0.214	···	···	···
NGC 4435	6	7.44	5.97 ($^{+1.4}_{-0.6}$)	0.209	0.671	1.72	3.94	4.13	···
NGC 4438	6	7.85	5.8	1.11	3.45	7.96	12.7	13.3	···
NGC 4477	3	1.78	0.928 (0.11)	0.0482	0.11	0.371	1.19	1.23	···
NGC 4596	3	1.5 (0.18)	0.953 (0.14)	0.0424	0.134	0.394	0.634	1.24	···
NGC 4697	6	1 (0.12)	0.623 (0.13)	0.0296	0.0888	0.26	0.654	0.911	···
NGC 4786	6	1.54	0.464 (0.096)	···	···	···	···	···	···
NGC 5208	6	2.73 (0.31)	1.33	···	···	···	···	···	···
NGC 5838	6	6.7	3.81	···	···	···	···	···	···
NGC 6861	7	18.2	2.44 ($^{+1.3}_{-0.24}$)	···	···	···	···	···	···
NGC 6958	6	37.6	14.6	···	···	···	···	···	···
PGC 43387	6	1.01 (0.12)	1 (0.19)	0.0881	0.15	0.275	0.374	0.514	···

Note. — New flux density measurements obtained via the methods described in sections 2.2 and 2.5.1. The second column lists the ALMA band from which the ALMA flux densities were measured. A 10% uncertainty for ALMA measurements, 10% for SPIRE, and 7% for PACS is assumed unless otherwise noted in parentheses.

Appendix B

Target Summaries

This appendix contains comprehensive results for our sample thus far. Numerical summaries of gas and dust properties are found in tables B.1 and B.2, respectively. Following the tables, a summary figure is shown for each observation in our sample. Each figure is organized as follows.

Left: Kinemetry results. From top to bottom: position angle (Γ), flattening (q), line-of-sight velocity (k_1), and deviation from circular rotation (k_5/k_1).

Top right: Voronoi-binned moment 0, 1, and 2 maps. Colormap minima/maxima are shown in the top right corner of each map, with a corresponding colorbar attached on the right side. Additionally, the beam size and a $1''$ scale bar are shown in the top left and bottom left corners of the moment 0 map, respectively. The dashed line through the moment 1 map illustrates the angle of the slice from which the PVD was taken.

Middle, from left to right: a histogram of flux density in each masked velocity channel; a PVD taken along the slice shown in the moment 1 map, and with a width equal to the beam FWHM; the averaged surface brightness profile (from kinemetry), with intensity (I/A_{beam}) units given on the left side and gas surface mass density (Σ'_{gas}) units given on the right.

Bottom right: the text shows the inherent velocity binning of the original data cube, as well as the target S/N used in the Voronoi binning process.

Table B.1. Gas Properties

Galaxy (1)	Transition (2)	R_d (pc) (3)	Δv_{CO} (km s^{-1}) (4)	$\Delta\Gamma$ (deg) (5)	$\tilde{q}$ (6)	I_{CO} (Jy km s^{-1}) (7)	L'_{CO} (10^6 K km s^{-1} pc^2) (8)	M_{gas} (10^7 $M_\odot$) (9)
NGC 383	CO(2−1)	1022	532	5.4	0.77	67.25 (6.73)	177 (23)	106 (13.6)
NGC 524	CO(2−1)	739	327	9.1	0.89	33.17 (3.33)	11.6 (2.5)	6.98 (1.51)
NGC 708	CO(2−1)	491	329	16.7	0.78	15.59 (1.56)	35.5 (4.5)	21.4 (2.74)
NGC 997	CO(2−1)	1856	465	5.4	0.9	93.22 (9.36)	482 (83)	290 (50.1)
NGC 1332	CO(2−1)	179	869	9.3	0.3	32.45 (3.25)	10.4 (2.1)	6.24 (1.25)
—	CO(2−1)	193	862	6.8	0.12	40.49 (4.06)	12.9 (2.6)	7.78 (1.55)
NGC 1380	CO(2−1)	361	559	3.0	0.31	57.19 (5.72)	10.8 (2.2)	6.5 (1.3)
NGC 1386	CO(1−0)	1533	377	22.3	0.38	75.25 (7.55)	50.1 (13)	21.1 (5.58)
NGC 1387	CO(1−0)	919	135	5.4	0.85	71.38 (7.14)	71.4 (20)	30.1 (8.24)
NGC 1684	CO(2−1)	2027	717	6.7	0.48	110.5 (11.1)	262 (33)	158 (19.7)
NGC 3258	CO(2−1)	160	543	2.6	0.86	20.63 (2.06)	12.8 (3.6)	7.73 (2.19)
NGC 3557	CO(2−1)	217	462	23.4	0.76	5.168 (0.517)	6.53 (1.5)	3.94 (0.927)
—	CO(2−1)	217	415	21.3	0.91	5.782 (0.579)	7.31 (1.7)	4.4 (1.04)
NGC 3607	CO(2−1)	802	507	68.9	0.86	110.6 (11.1)	35.0 (6.7)	21.1 (4.05)
NGC 4061	CO(2−1)	1010	738	9.6	0.61	19.23 (1.93)	124 (13)	74.9 (7.78)
NGC 4435	CO(2−1)	153	362	4.7	0.6	77.0 (7.7)	13.0 (1.5)	7.84 (0.925)
—	CO(2−1)	208	419	1.4	0.38	77.58 (7.76)	13.1 (1.5)	7.9 (0.931)
NGC 4438	CO(2−1)	1589	732	19.3	0.38	531.8 (53.3)	90.1 (11)	54.3 (6.41)
NGC 4477	CO(1−0)	188	347	12.1	0.94	6.888 (0.691)	3.8 (0.66)	1.6 (0.277)
NGC 4596	CO(1−0)	249	277	15.8	0.79	9.09 (0.911)	4.89 (0.84)	2.06 (0.355)
NGC 4697	CO(2−1)	150	418	2.1	0.3	10.32 (1.03)	0.868 (0.14)	0.523 (0.087)
NGC 4786	CO(2−1)	160	460	1.4	0.9	7.147 (0.715)	24.7 (4.2)	14.9 (2.56)
NGC 5208	CO(2−1)	7602	800	0.8	0.18	65.04 (6.54)	471 (81)	284 (48.9)
NGC 5838	CO(2−1)	196	823	3.0	0.45	28.4 (2.84)	9.93 (1.7)	5.98 (1.03)
NGC 6861	CO(2−1)	784	1012	3.7	0.29	85.05 (8.51)	40.5 (15)	24.4 (9.14)
—	CO(3−2)	797	1034	5.1	0.29	93.07 (9.31)	19.7 (7.4)	17.0 (6.35)
NGC 6958	CO(2−1)	331	443	4.9	0.77	218.2 (21.9)	246 (42)	148 (25.5)
PGC 43387	CO(2−1)	1117	490	2.1	0.67	16.97 (1.7)	122 (21)	73.3 (12.6)

Note. — Some derived gas properties from ALMA moment maps. Col. (3): radius of the binned moment map in physical units. Col. (4): width of the detected line emission. Col. (5): range of position angles from the KINEMETRY to the moment 1 map. Col. (6): median flattening of the moment 1 map. Col. (7): intensity of the observed emission line. Col. (8): luminosity of the observed emission line. Col. (9): derived total gas mass as described in section 2.4.

Table B.2. Dust Properties

Galaxy (1)	$M_{\rm dust}$ ($10^6\ M_\odot$) (2)	$T_{\rm dust}$ (K) (3)	β (4)
NGC 0383	12.4 (1.9)	26.5 (1.8)	1.46 (0.18)
NGC 0524	1.08 (0.39)	29.2 (2.4)	1.68 (0.18)
NGC 0708	1.76 (0.021)	21.4 (0.2)	3.43 (0.01)
NGC 0997	25.3 (3.6)	24.1 (0.7)	2.0*
NGC 1332	1.69 (0.18)	21.7 (0.6)	2.54 (0.08)
NGC 1380	0.987 (0.071)	25.4 (0.7)	2.29 (0.12)
NGC 1386	2.76 (0.24)	29.3 (0.7)	1.71 (0.05)
NGC 1387	3.95 (0.28)	26.4 (0.6)	1.83 (0.07)
NGC 1684	25.1 (3.9)	24.1 (1.2)	1.9 (0.16)
NGC 3258	1.7 (1.7)	23.5 (2.3)	2.0*
NGC 3268	0.0964 (0.54)	33.5 (5.5)	2.0*
NGC 3557	0.551 (0.12)	39.3 (3.8)	1.02 (0.11)
NGC 3607	3.73 (0.36)	19.8 (0.6)	3.2 (0.12)
NGC 3862	...	...	...
NGC 4061	3.6 (6.8)	50.0 (9.1)	0.88 (0.24)
NGC 4435	1.97 (0.24)	25.2 (1.1)	1.99 (0.12)
NGC 4438	6.58 (0.34)	21.2 (0.2)	2.64 (0.04)
NGC 4477	0.448 (0.05)	22.4 (1.3)	2.46 (0.24)
NGC 4596	0.223 (0.02)	29.3 (0.7)	1.8*
NGC 4697	0.133 (0.017)	25.8 (1.3)	2.24 (0.14)
NGC 4786	3.52 (2.0)	26.5 (3.9)	2.25 (0.34)
NGC 5208	30.8 (14)	22.6 (1.7)	2.37 (0.2)
NGC 5838	0.904 (0.1)	31.0 (1.0)	1.5 (0.08)
NGC 6861	4.38 (0.49)	23.3 (0.7)	2.34 (0.11)
NGC 6958	4.13 (0.54)	36.3 (1.7)	0.847 (0.09)
PGC 43387	16.6 (3.0)	23.0 (1.3)	1.87 (0.12)

Note. — Parameters for modified blackbodies fit to the SED for each target, with the exception of NGC 3862 where the data were too difficult to fit, probably due to a contaminating source in the Herschel data.

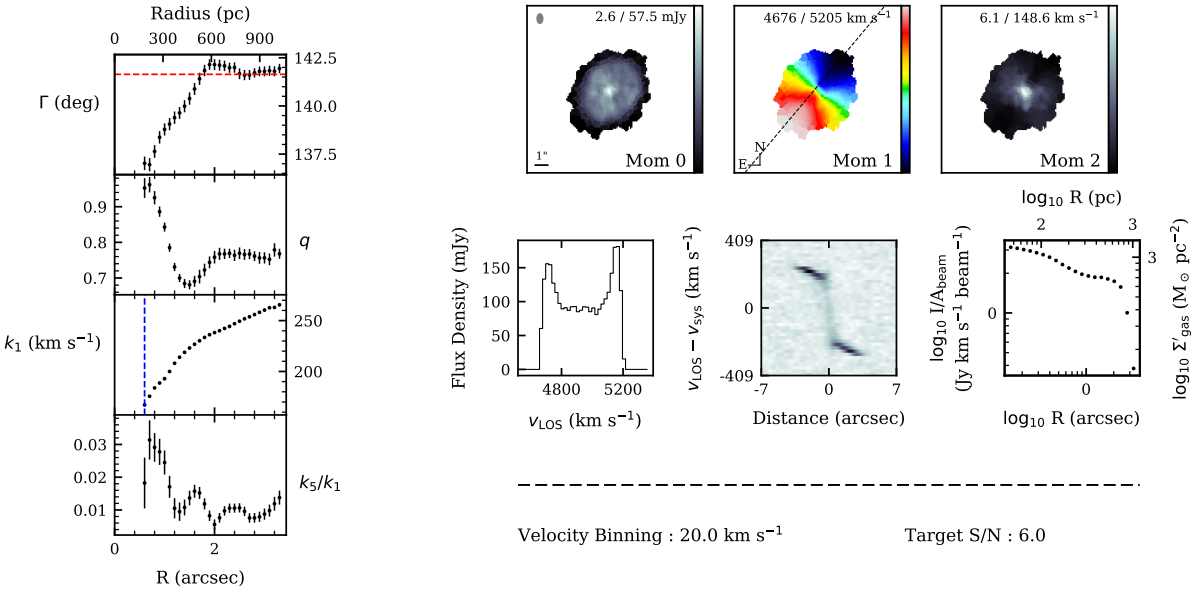

Figure B.1 NGC 383 Summary (2015.1.00419.S)

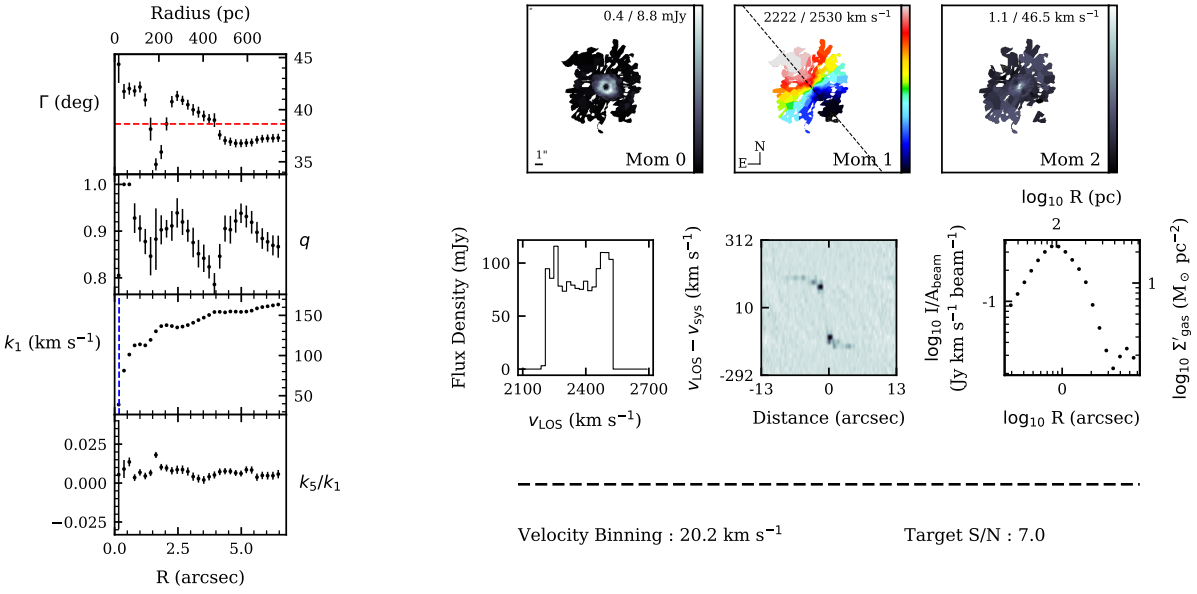

Figure B.2 NGC 524 Summary (2015.1.00466.S)

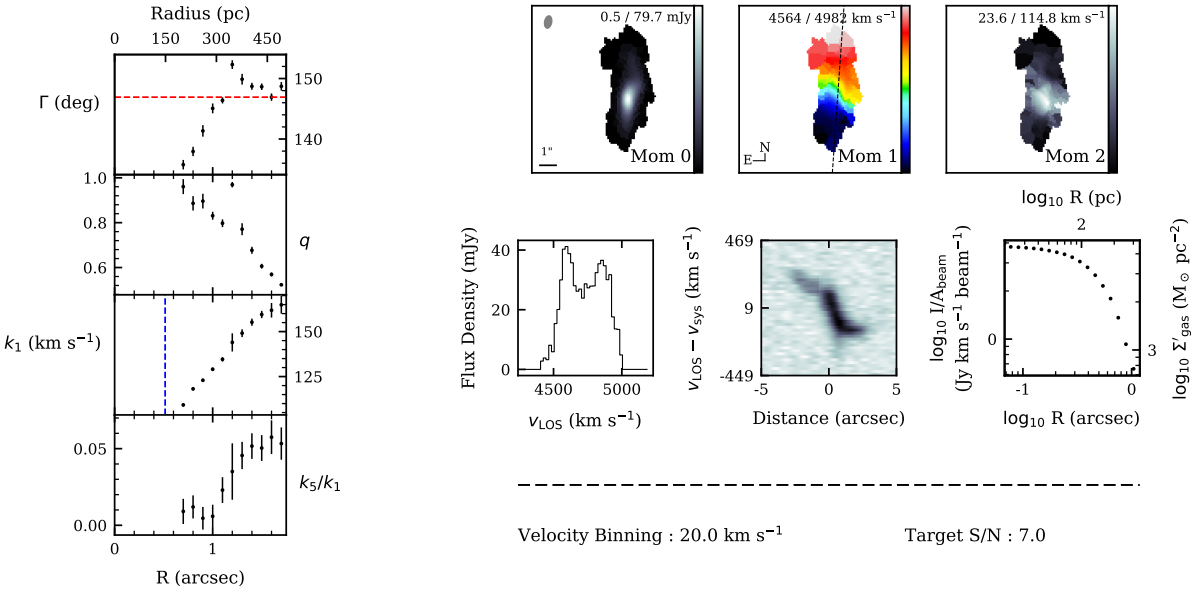

Figure B.3 NGC 708 Summary (2015.1.00598.S)

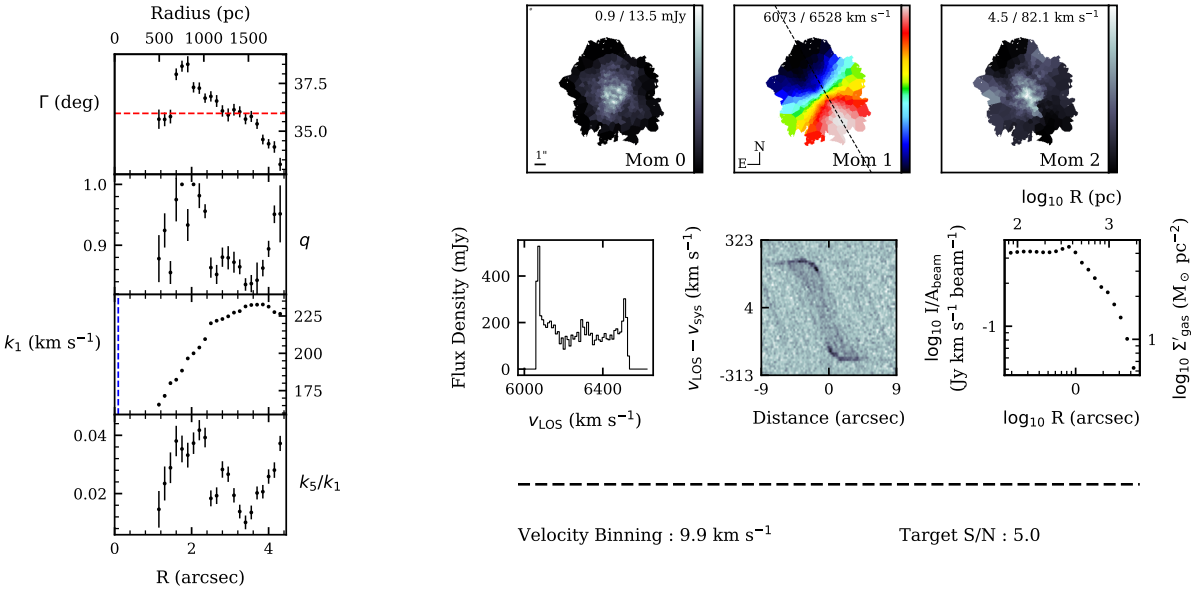

Figure B.4 NGC 997 Summary (2015.1.00187.S)

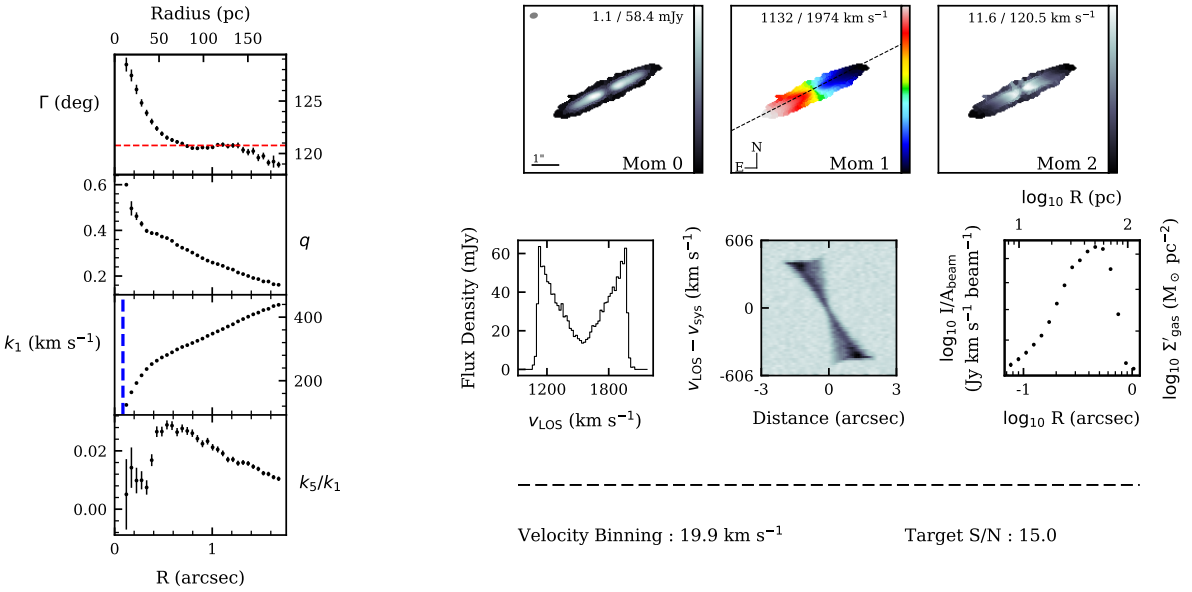

Figure B.5 NGC 1332 Summary (2013.1.00229.S)

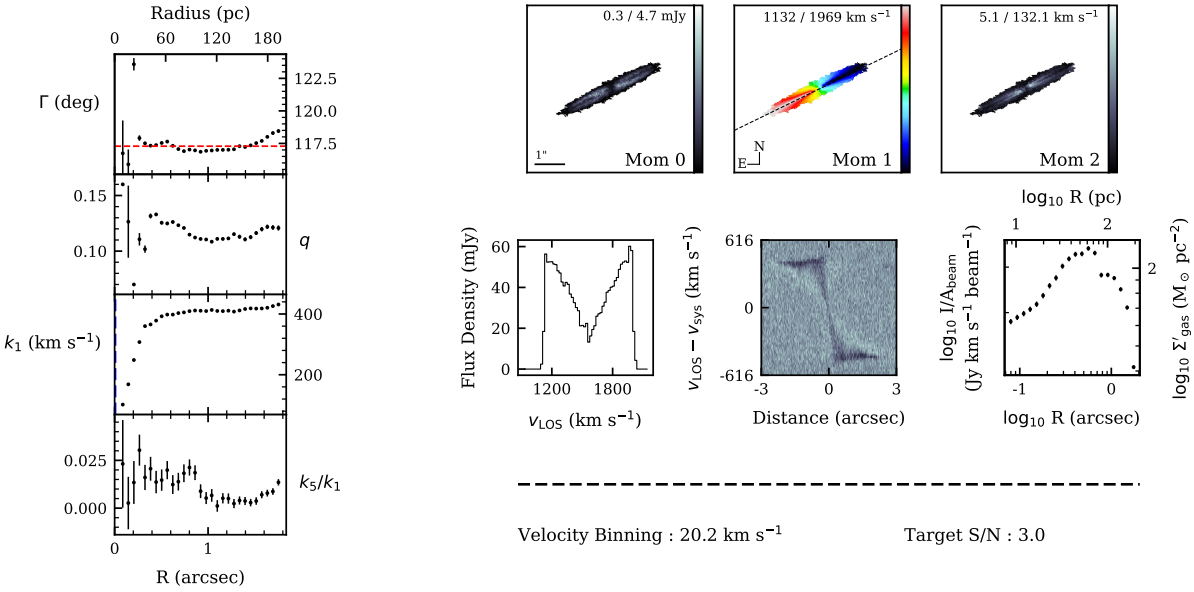

Figure B.6 NGC 1332 Summary (2015.1.00896.S)

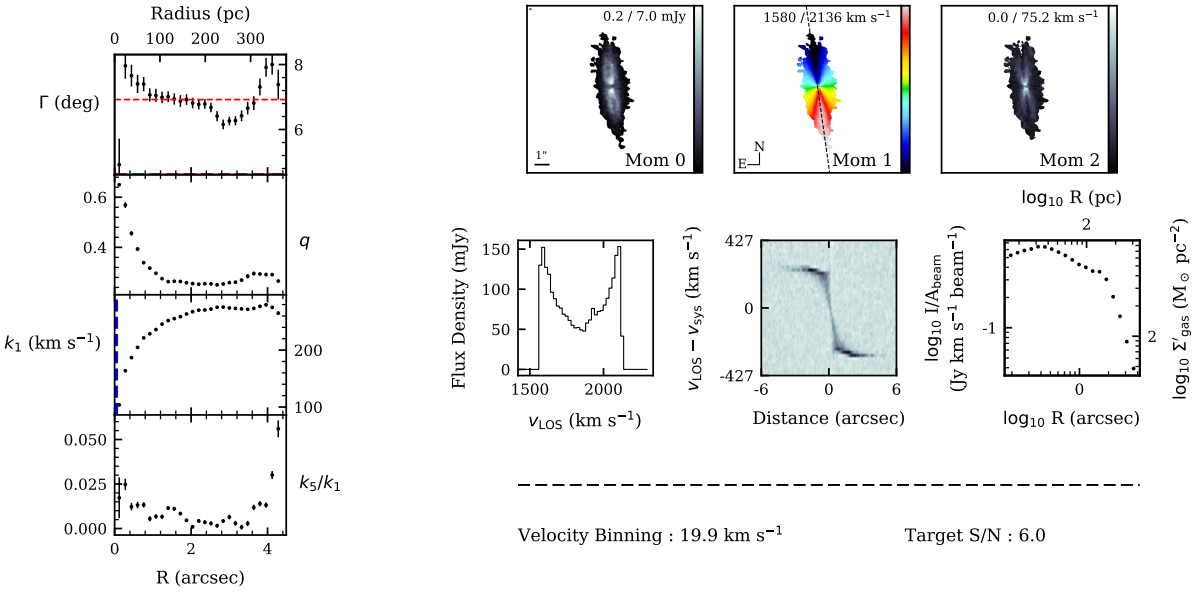

Figure B.7 NGC 1380 Summary (2013.1.00229.S)

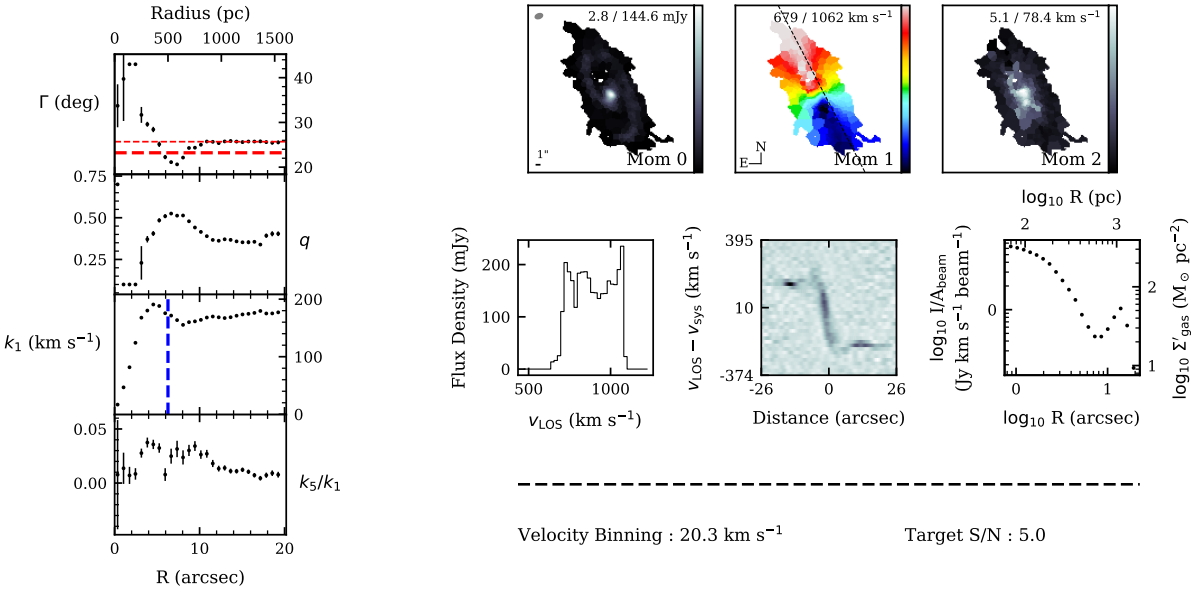

Figure B.8 NGC 1386 Summary (2015.1.00497.S)

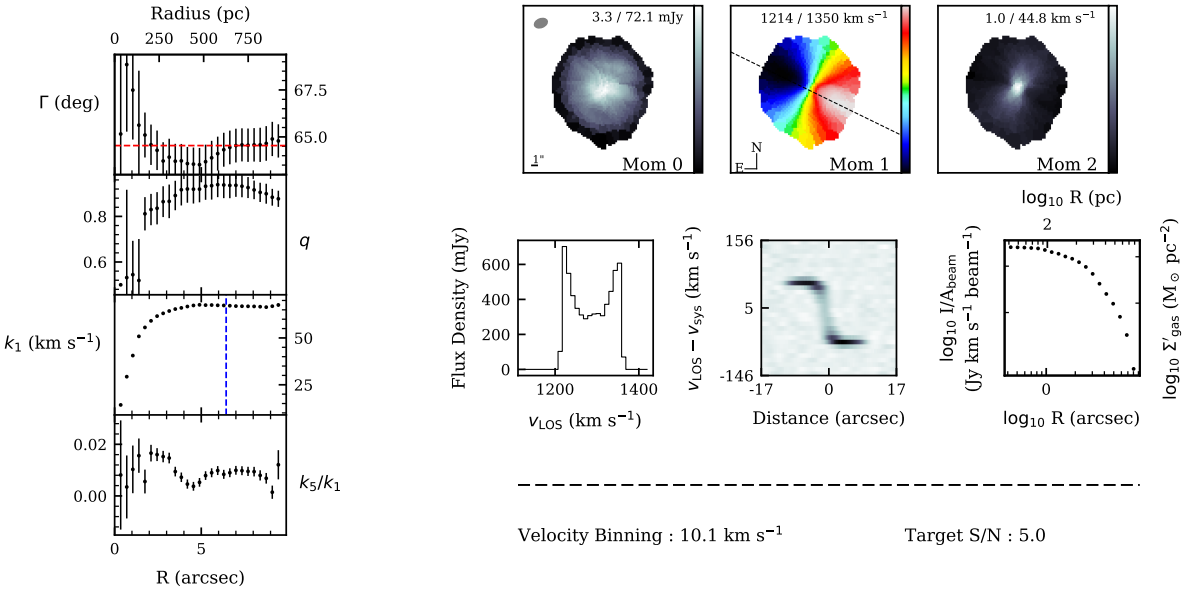

Figure B.9 NGC 1387 Summary (2015.1.00497.S)

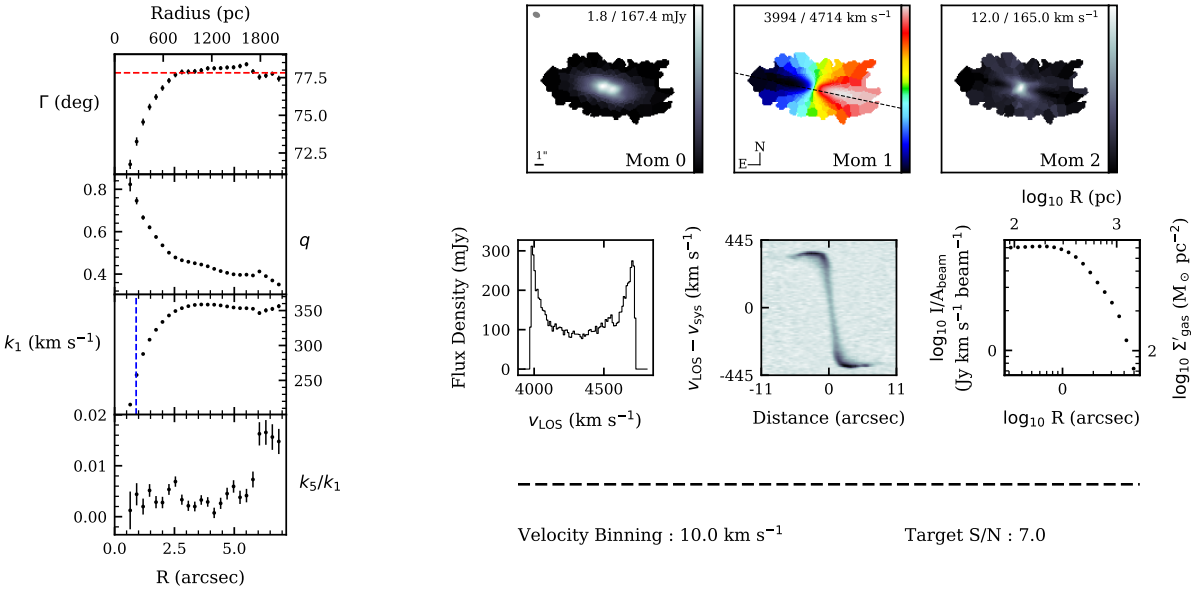

Figure B.10 NGC 1684 Summary (2015.1.00187.S)

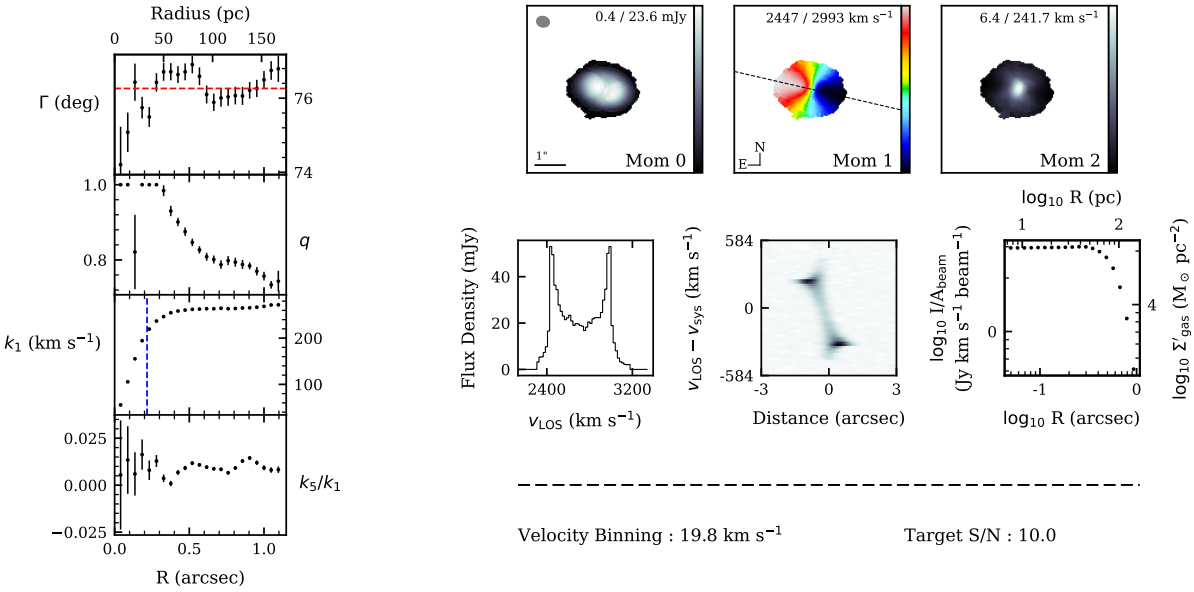

Figure B.11 NGC 3258 Summary (2013.1.00229.S)

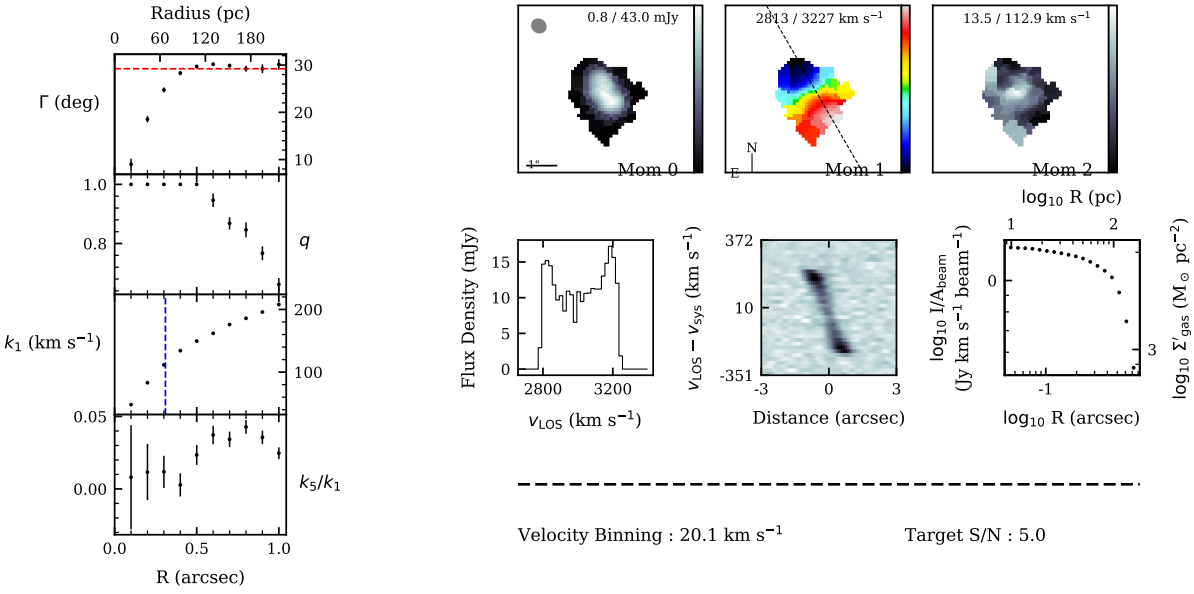

Figure B.12 NGC 3557 Summary (2015.1.01572.S)

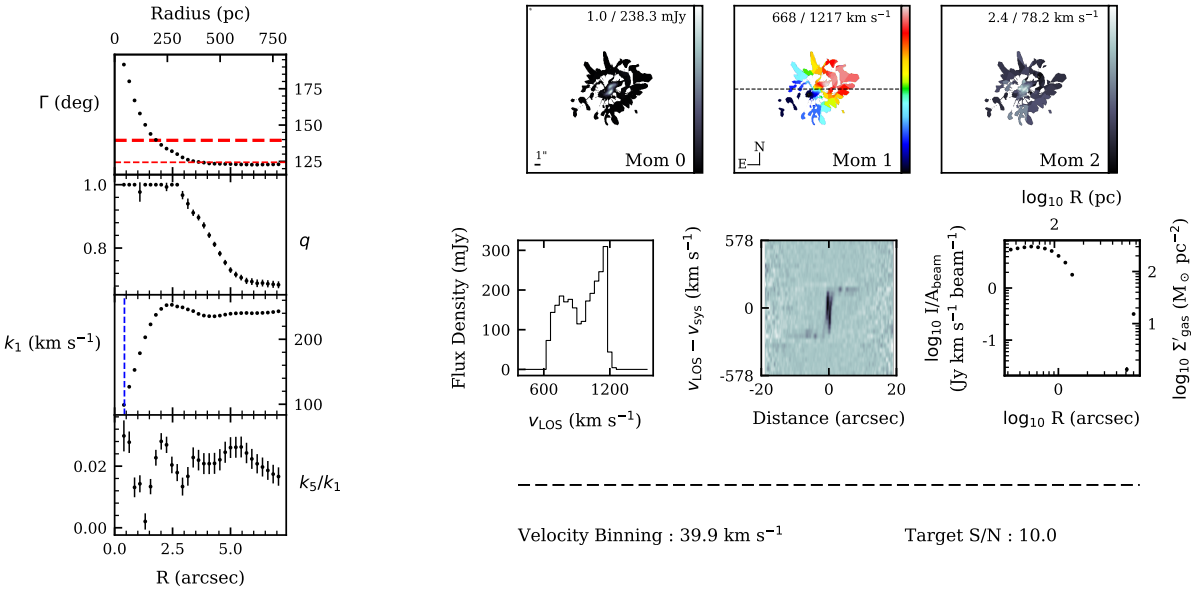

Figure B.13 NGC 3607 Summary (2015.1.00598.S)

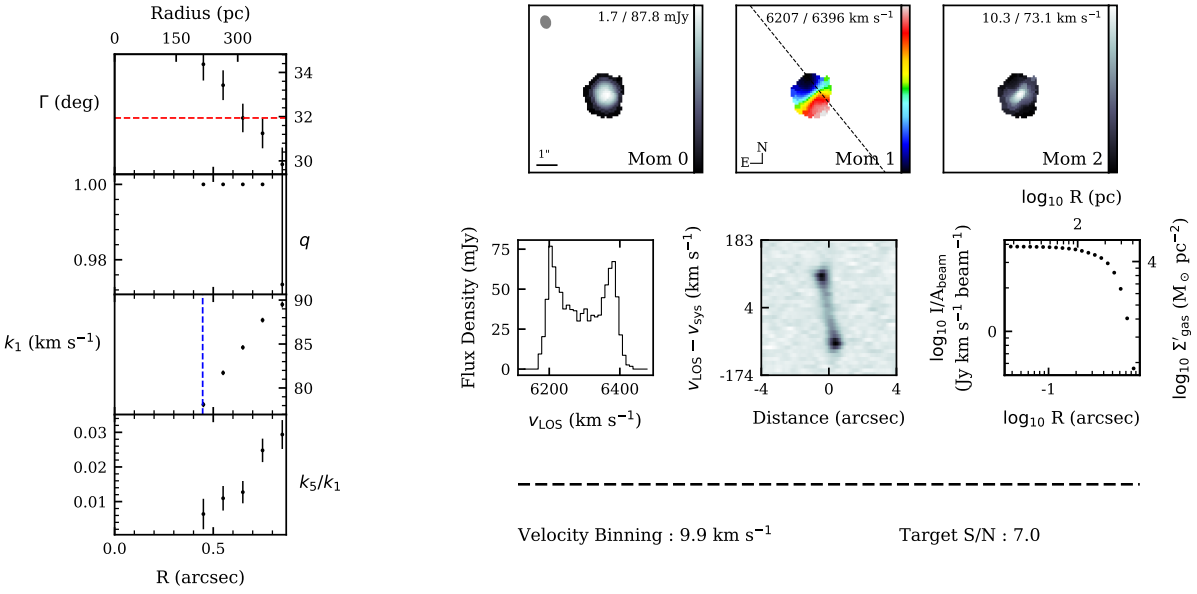

Figure B.14 NGC 3862 Summary (2015.1.00598.S)

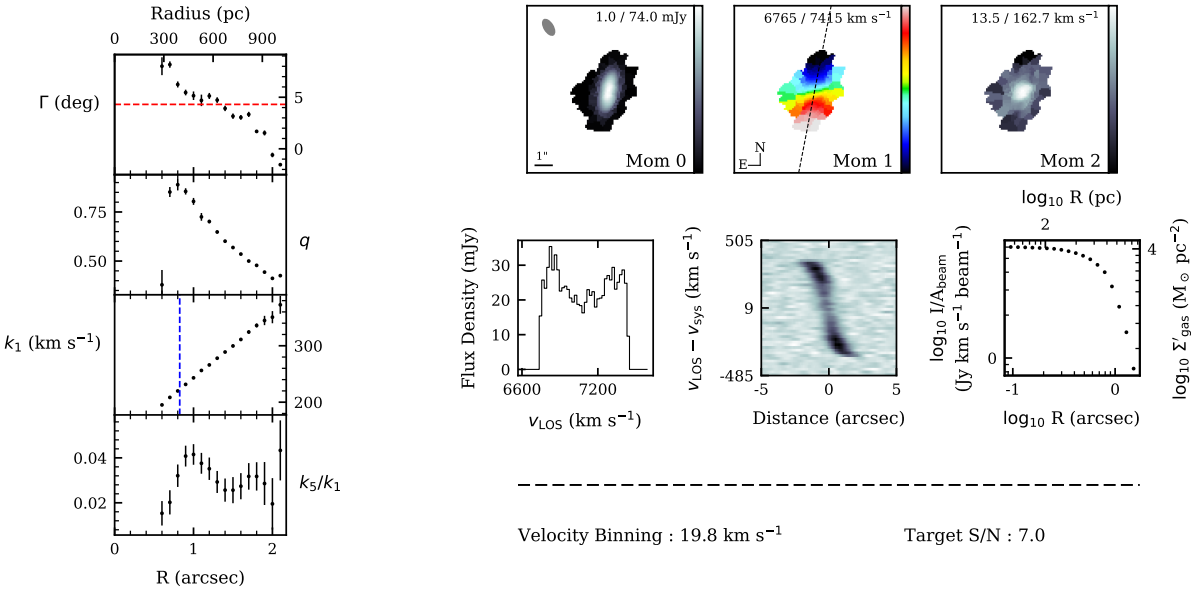

Figure B.15 NGC 4061 Summary (2015.1.00598.S)

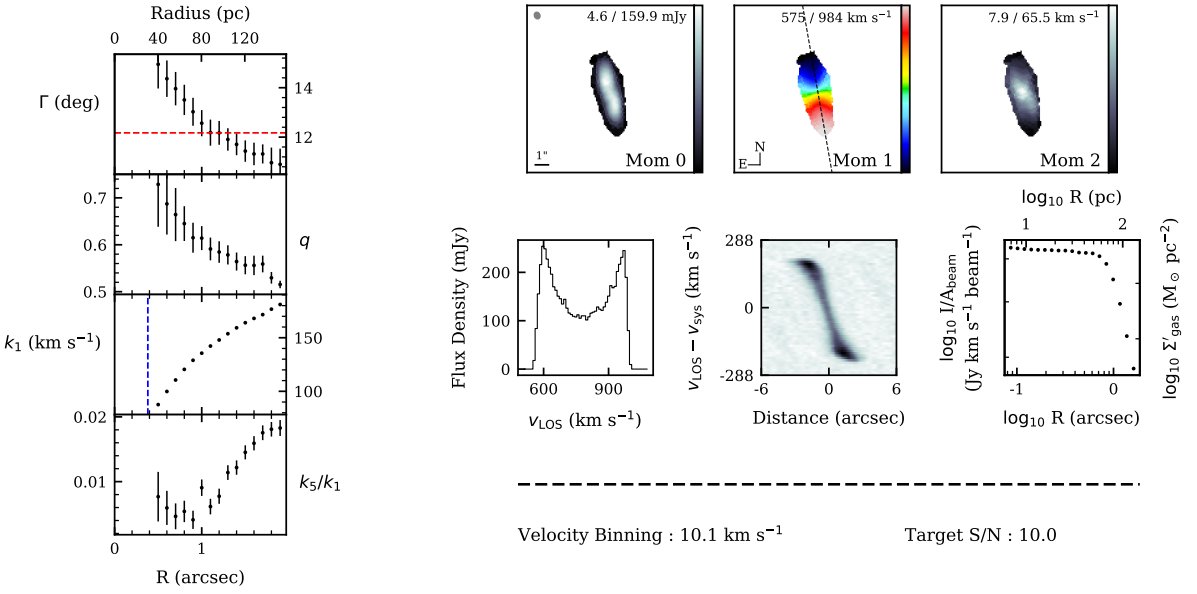

Figure B.16 NGC 4435 Summary (2015.1.00598.S)

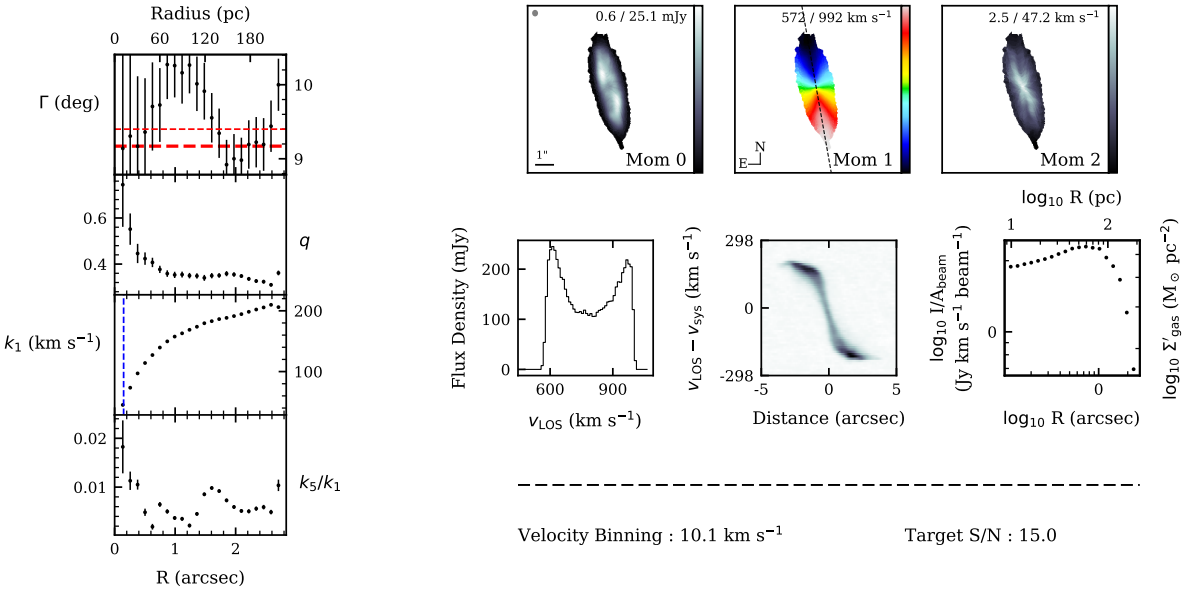

Figure B.17 NGC 4435 Summary (2017.1.00301.S)

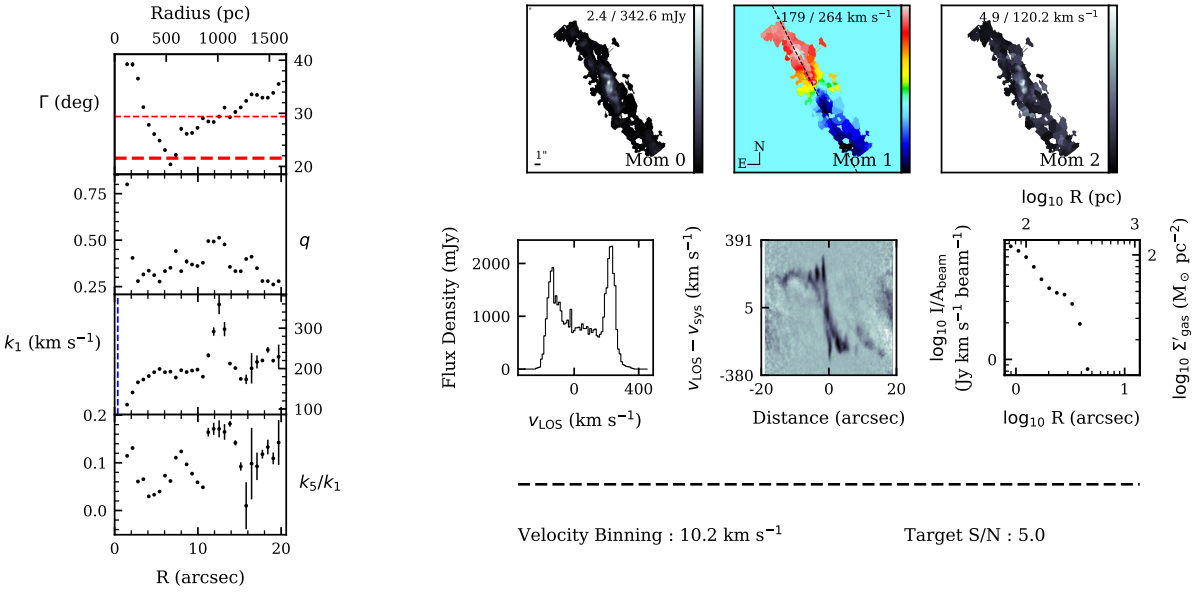

Figure B.18 NGC 4438 Summary (2015.1.00598.S)

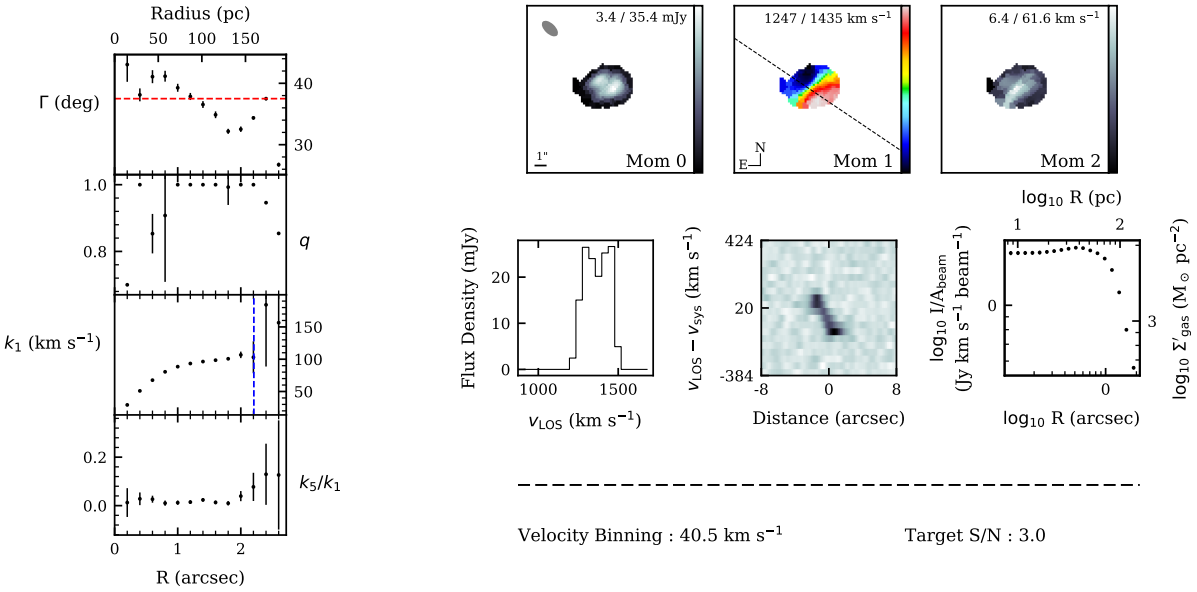

Figure B.19 NGC 4477 Summary (2015.1.00989.S)

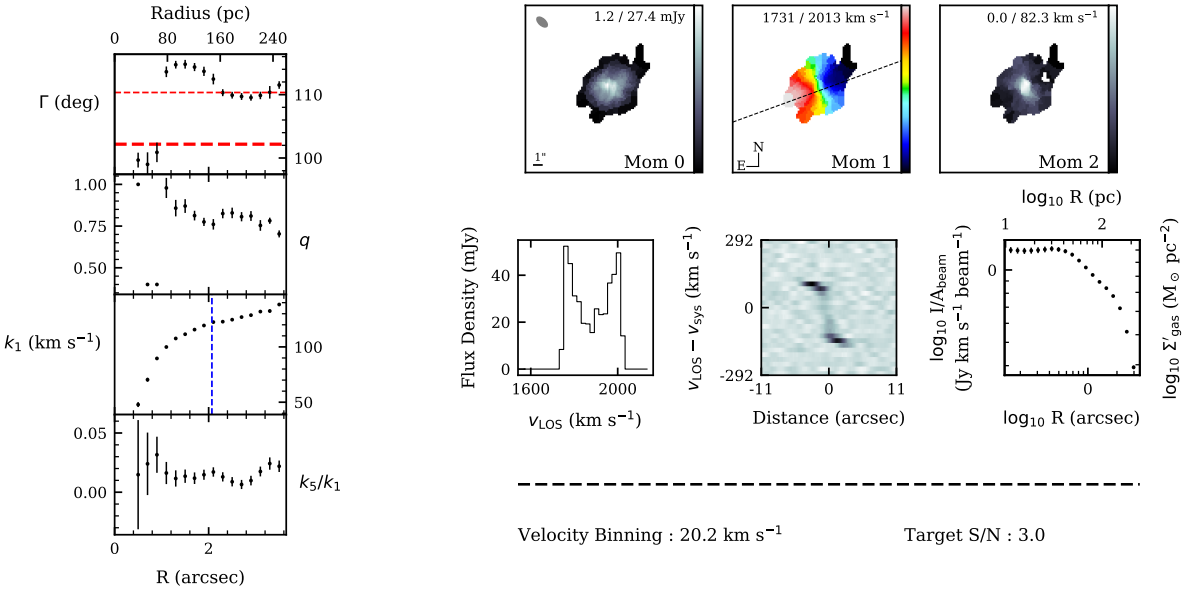

Figure B.20 NGC 4596 Summary (2015.1.00989.S)

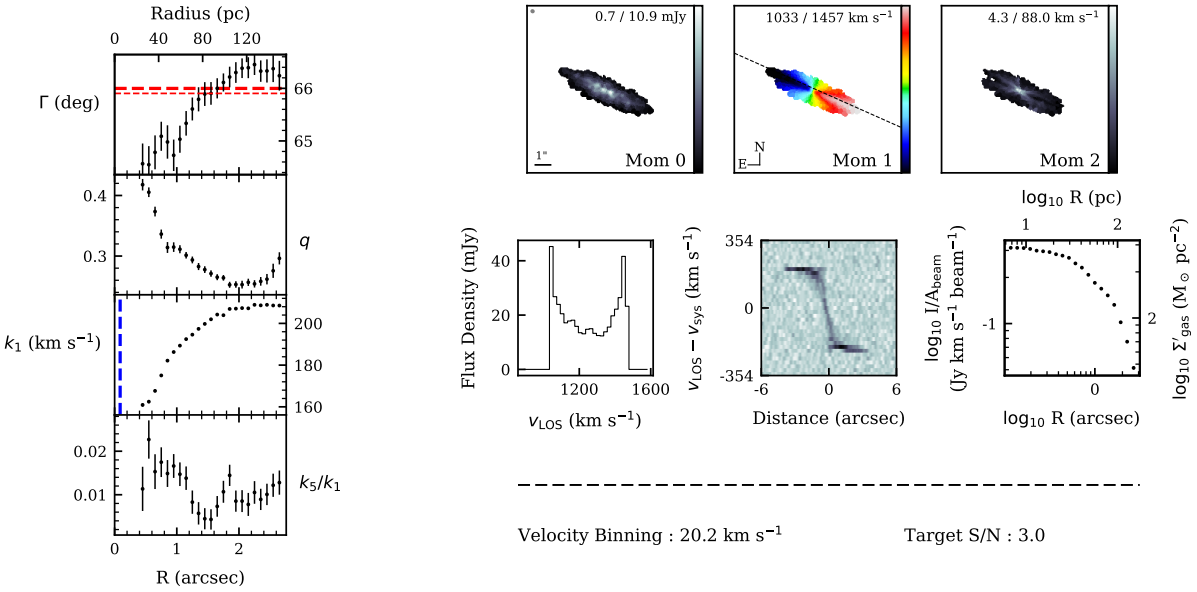

Figure B.21 NGC 4697 Summary (2015.1.00878.S)

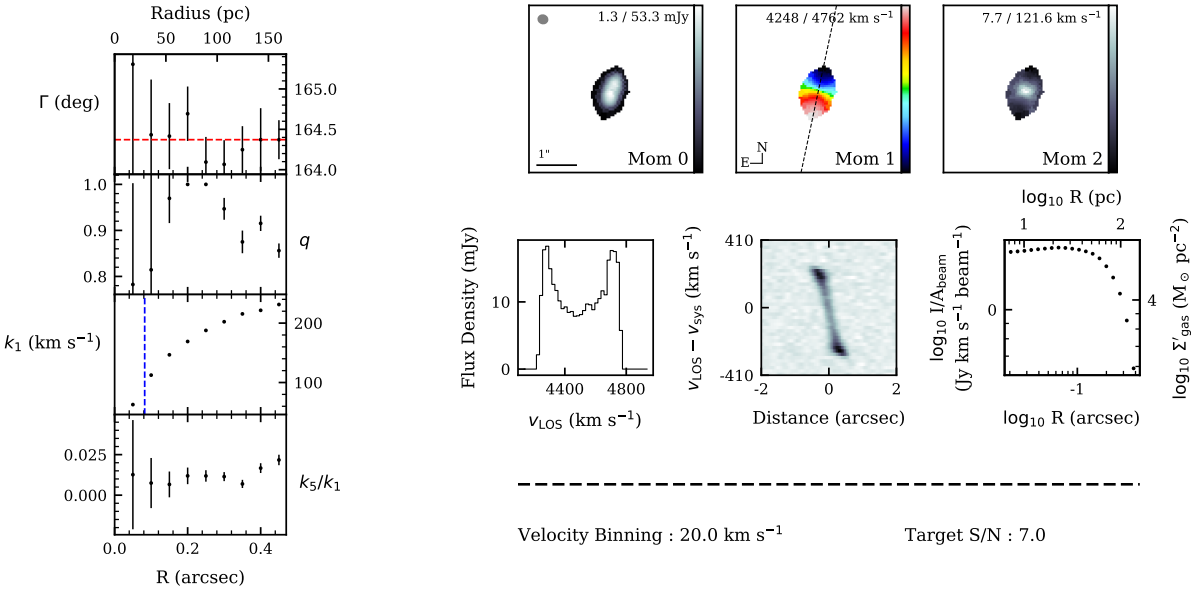

Figure B.22 NGC 4786 Summary (2015.1.00878.S)

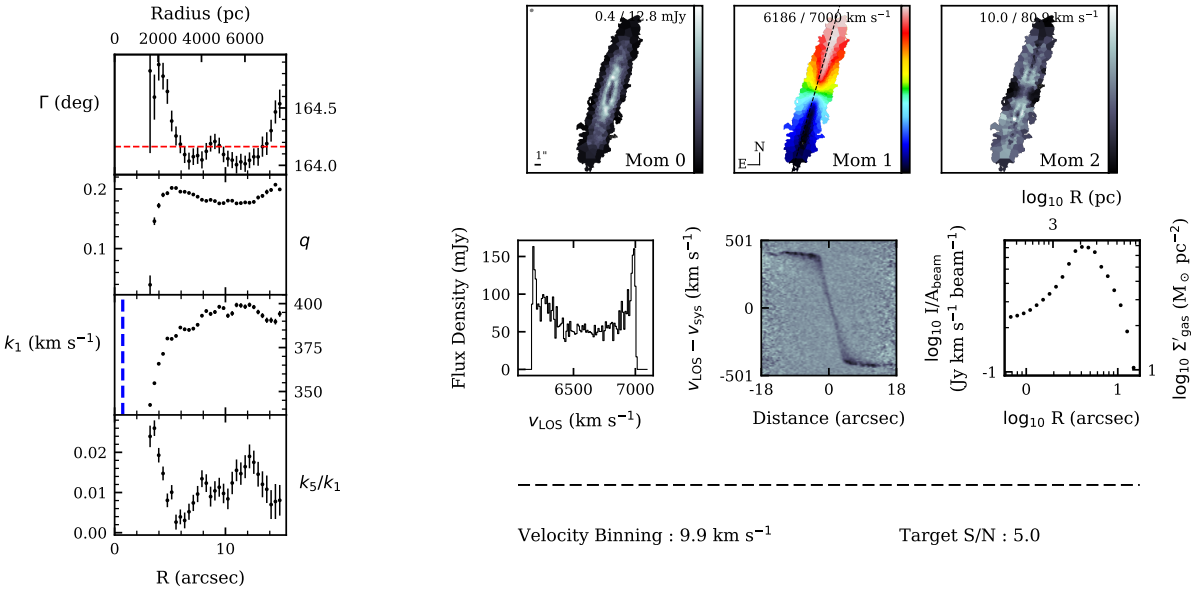

Figure B.23 NGC 5208 Summary (2015.1.00187.S)

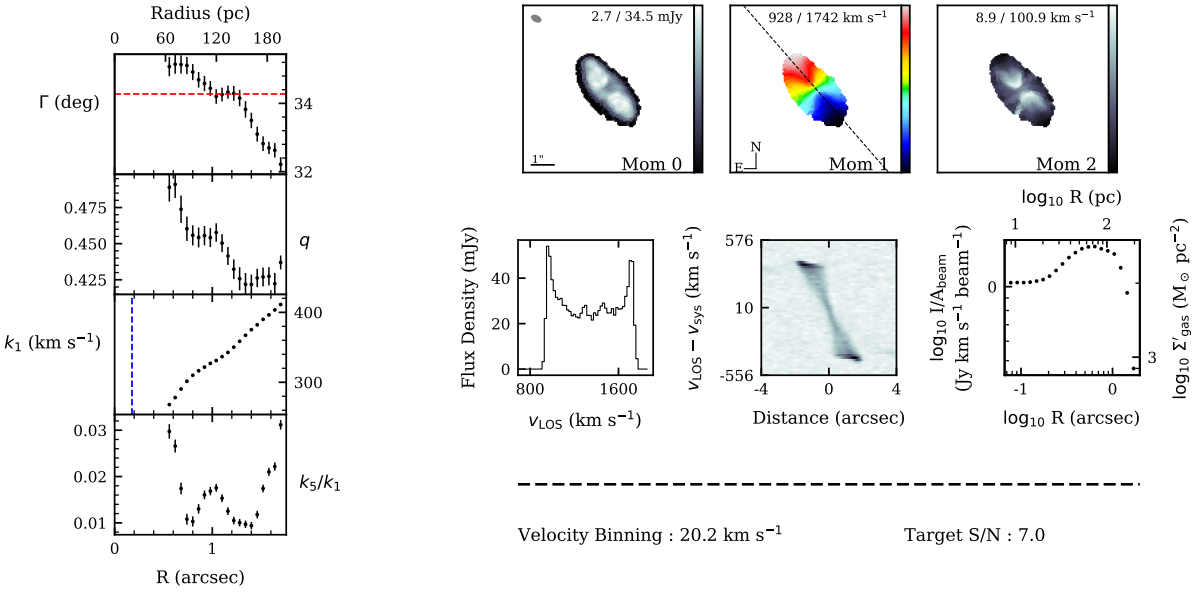

Figure B.24 NGC 5838 Summary (2015.1.00878.S)

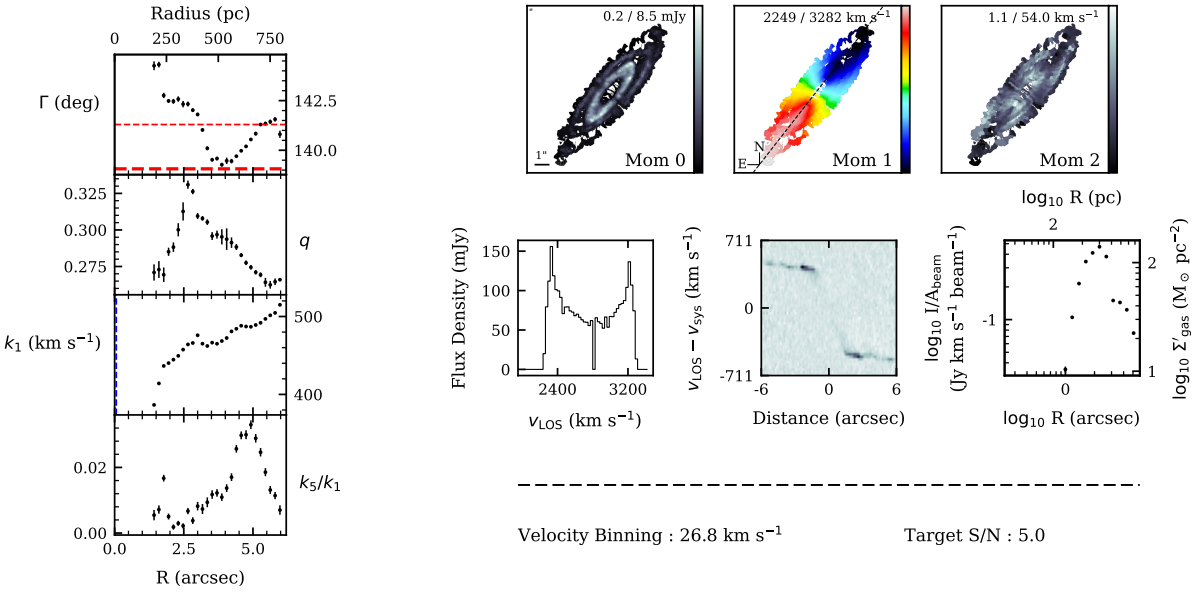

Figure B.25 NGC 6861 Summary (2016.1.01135.S)

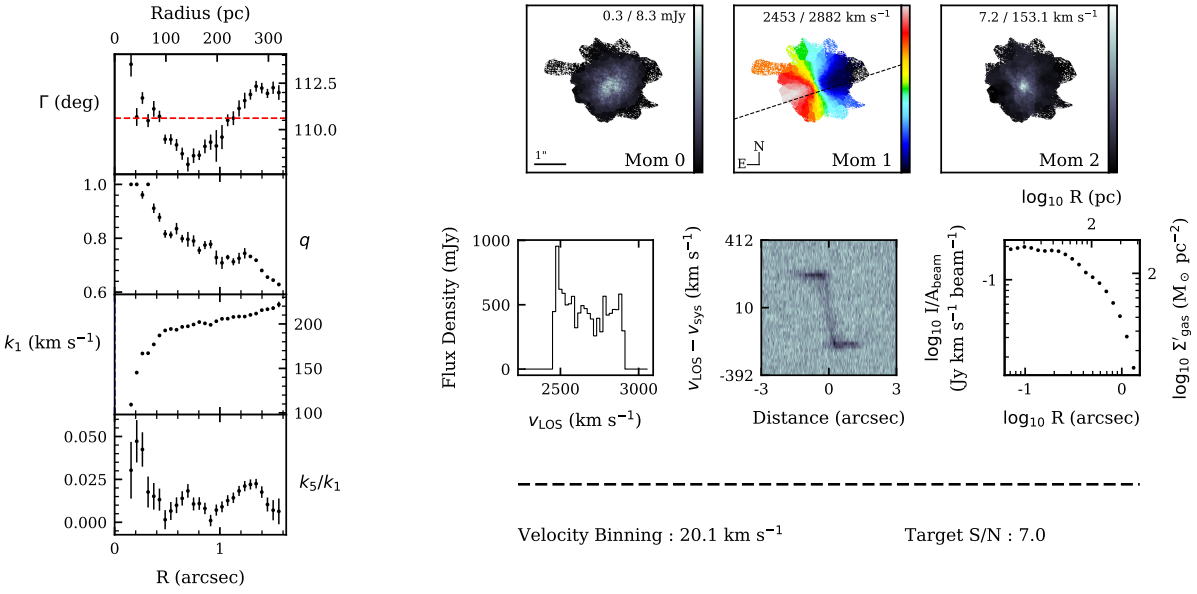

Figure B.26 NGC 6958 Summary (2015.1.00466.S)

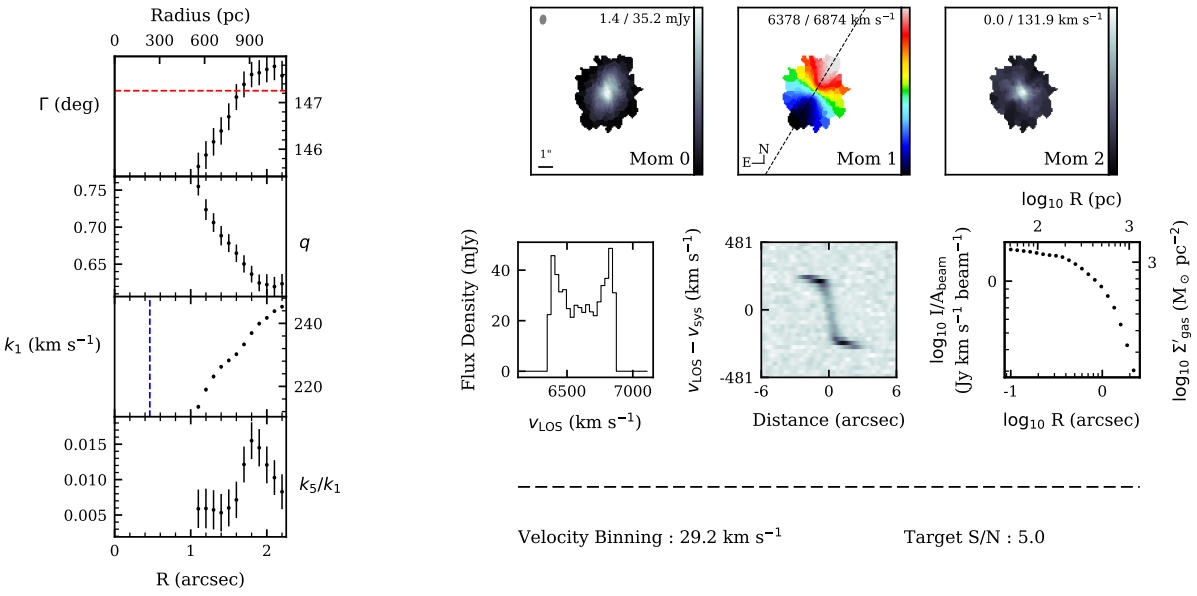

Figure B.27 PGC 43387 Summary (2015.1.00598.S)

Bibliography

Alatalo, K., et al. 2013, MNRAS, 432, 1796

Baan, W. A., & Klöckner, H. R. 2006, A&A, 449, 559

Bacon, R., et al. 2001, MNRAS, 326, 23

Barth, A. J., Boizelle, B. D., Darling, J., Baker, A. J., Buote, D. A., Ho, L. C., & Walsh, J. L. 2016, ApJ, 822, L28

Blakeslee, J. P., et al. 2009, ApJ, 694, 556

Bock, D. C. J. 2006, in Astronomical Society of the Pacific Conference Series, Vol. 356, Revealing the Molecular Universe: One Antenna is Never Enough, ed. D. C. Backer, J. M. Moran, & J. L. Turner, 17

Boizelle, B. D., Barth, A. J., Darling, J., Baker, A. J., Buote, D. A., Ho, L. C., & Walsh, J. L. 2017, ApJ, 845, 170

Boizelle, B. D., Barth, A. J., Walsh, J. L., Buote, D. A., Baker, A. J., Darling, J., & Ho, L. C. 2019, ApJ, 881, 10

Boizelle, B. D., et al. 2021, ApJ, 908, 19

Bolatto, A. D., Wolfire, M., & Leroy, A. K. 2013, ARA&A, 51, 207

Briggs, D. S. 1995, PhD thesis, New Mexico Institute of Mining and Technology

Brown, M. J. I., Jannuzi, B. T., Floyd, D. J. E., & Mould, J. R. 2011, ApJ, 731, L41

Brown, M. J. I., et al. 2017, ApJ, 847, 136

Cappellari, M. 2002, MNRAS, 333, 400

Cappellari, M., & Copin, Y. 2003, MNRAS, 342, 345

Cappellari, M., et al. 2011, MNRAS, 413, 813

Carilli, C. L., & Walter, F. 2013, ARA&A, 51, 105

CASA Team et al. 2022, PASP, 134, 114501

Clemens, M. S., et al. 2010, A&A, 518, L50

Combes, F., Young, L. M., & Bureau, M. 2007, MNRAS, 377, 1795

Condon, J. J., Cotton, W. D., & Broderick, J. J. 2002, AJ, 124, 675

Cox, A. L., & Sparke, L. S. 2004, AJ, 128, 2013

Cutri, R. M., et al. 2012, Explanatory Supplement to the WISE All-Sky Data Release Products

Davis, T. A., & Bureau, M. 2016, MNRAS, 457, 272

Davis, T. A., Bureau, M., Onishi, K., Cappellari, M., Iguchi, S., & Sarzi, M. 2017, MNRAS, 468, 4675

Davis, T. A., et al. 2011, MNRAS, 417, 882

—. 2013, MNRAS, 429, 534

de Vaucouleurs, G., de Vaucouleurs, A., Corwin, Herold G., J., Buta, R. J., Paturel, G., & Fouque, P. 1991, Third Reference Catalogue of Bright Galaxies

de Zeeuw, P. T., et al. 2002, MNRAS, 329, 513

di Serego Alighieri, S., et al. 2007, A&A, 474, 851

—. 2013, A&A, 552, A8

Disney, M. J., & Wall, J. V. 1977, MNRAS, 179, 235

Draine, B. T. 1989, in Infrared Spectroscopy in Astronomy, ed. E. Böhm-Vitense, 93

Draine, B. T. 2003, ARAA, 41, 241

Draine, B. T., & Salpeter, E. E. 1979, ApJ, 231, 77

Dressel, L. L., & Condon, J. J. 1978, ApJS, 36, 53

Duchon, J. 1977, in Constructive Theory of Functions of Several Variables, ed. W. Schempp & K. Zeller (Berlin, Heidelberg: Springer Berlin Heidelberg), 85–100

Exter, K. 2017, Quick-Start Guide to Herschel-PACS: The Photometer

Falcón-Barroso, J., et al. 2006, MNRAS, 369, 529

Fomalont, E., et al. 2014, The Messenger, 155, 19

Foreman-Mackey, D., Hogg, D. W., Lang, D., & Goodman, J. 2013, PASP, 125, 306

Ghosh, K. K., Swartz, D. A., Tennant, A. F., Wu, K., & Saripalli, L. 2005, ApJ, 623, 815

Hirota, A., et al. 2018, PASJ, 70, 73

Hubble, E. P. 1926, ApJ, 64, 321

IRAC Instrument and Instrument Support Teams. 2021, IRAC Instrument Handbook

Jensen, J. B., et al. 2021, ApJS, 255, 21

John, F. 2014, Extremum Problems with Inequalities as Subsidiary Conditions, ed. G. Giorgi & T. H. Kjeldsen (Basel: Springer Basel), 197–215

Knapp, G. R., Guhathakurta, P., Kim, D.-W., & Jura, M. A. 1989, ApJS, 70, 329

Kokusho, T., Kaneda, H., Bureau, M., Suzuki, T., Murata, K., Kondo, A., & Yamagishi, M. 2017, A&A, 605, A74

Kokusho, T., et al. 2019, A&A, 622, A87

Kormendy, J., & Ho, L. C. 2013, ARA&A, 51, 511

Krajnović, D., Cappellari, M., de Zeeuw, P. T., & Copin, Y. 2006, MNRAS, 366, 787

Krajnović, D., et al. 2011, MNRAS, 414, 2923

Leipski, C., Falcke, H., Bennert, N., & Hüttemeister, S. 2006, A&A, 455, 161

Leroy, A., Bolatto, A. D., Simon, J. D., & Blitz, L. 2005, ApJ, 625, 763

Liu, L., Bureau, M., Blitz, L., Davis, T. A., Onishi, K., Smith, M., North, E., & Iguchi, S. 2021, MNRAS, 505, 4048

Makarov, D., Prugniel, P., Terekhova, N., Courtois, H., & Vauglin, I. 2014, A&A, 570, A13

Mandel, K. S., Narayan, G., & Kirshner, R. P. 2011, ApJ, 731, 120

Markwardt, C. B. 2009, in Astronomical Society of the Pacific Conference Series, Vol. 411, Astronomical Data Analysis Software and Systems XVIII, ed. D. A. Bohlender, D. Durand, & P. Dowler, 251

Martig, M., et al. 2013, MNRAS, 432, 1914

Mauch, T., Murphy, T., Buttery, H. J., Curran, J., Hunstead, R. W., Piestrzynski, B., Robertson, J. G., & Sadler, E. M. 2003, MNRAS, 342, 1117

Moshir, M. e. 1990, IRAS Faint Source Catalogue, 0

Müller, T., Okumura, K., & Klaas, U. 2011, 19

Mundell, C. G., Ferruit, P., Nagar, N., & Wilson, A. S. 2009, ApJ, 703, 802

Murphy, T., et al. 2010, MNRAS, 402, 2403

Nagar, N. M., Falcke, H., & Wilson, A. S. 2005, A&A, 435, 521

North, E. V., et al. 2019, MNRAS, 490, 319

Putman, M. E., Zheng, Y., Price-Whelan, A. M., Grcevich, J., Johnson, A. C., Tollerud, E., & Peek, J. E. G. 2021, ApJ, 913, 53

Ruffa, I., et al. 2019a, MNRAS, 489, 3739

—. 2019b, MNRAS, 484, 4239

Sandstrom, K. M., et al. 2013, ApJ, 777, 5

Sarzi, M., et al. 2006, MNRAS, 366, 1151

Serra, P., et al. 2012, MNRAS, 422, 1835

Tarenghi, M. 2008, Ap&SS, 313, 1

Teague, R. 2019, Research Notes of the AAS, 3, 74

Temi, P., Brighenti, F., Mathews, W. G., & Bregman, J. D. 2004, ApJS, 151, 237

Tonry, J. L., Dressler, A., Blakeslee, J. P., Ajhar, E. A., Fletcher, A. B., Luppino, G. A., Metzger, M. R., & Moore, C. B. 2001, ApJ, 546, 681

Tran, H. D., Tsvetanov, Z., Ford, H. C., Davies, J., Jaffe, W., van den Bosch, F. C., & Rest, A. 2001, AJ, 121, 2928

Utomo, D., Blitz, L., Davis, T., Rosolowsky, E., Bureau, M., Cappellari, M., & Sarzi, M. 2015, ApJ, 803, 16

Utomo, D., et al. 2017, ApJ, 849, 26

—. 2018, ApJ, 861, L18

Valtchanov, I. 2017, Quick-Start Guide to Herschel-SPIRE

—. 2018, SPIRE Handbook

van de Voort, F., Davis, T. A., Kereš, D., Quataert, E., Faucher-Giguère, C.-A., & Hopkins, P. F. 2015, MNRAS, 451, 3269

van den Bosch, R. C. E. 2016, ApJ, 831, 134

Virtanen, P., et al. 2020, Nature Methods, 17, 261

Vollmer, B., Thierbach, M., & Wielebinski, R. 2004, A&A, 418, 1

Young, L. M., et al. 2011, MNRAS, 414, 940

Index